Physics of Fluids

REVIEW ARTICLE | APRIL 21 2021

On the lattice Boltzmann method and its application to turbulent, multiphase flows of various fluids including cryogens: A review

Special Collection: Special Issue on the Lattice Boltzmann Method

K. J. Petersen ; J. R. Brinkerhoff

Check for updates

Physics of Fluids 33, 041302 (2021)
https://doi.org/10.1063/5.0046938

View Online
Export Citation

Articles You May Be Interested In

Highly accurate simplified lattice Boltzmann method

Physics of Fluids (October 2018)

Carrier conduction mechanisms in MIS capacitors with ultra-thin Al_2O_3 at cryogenic temperatures

Appl. Phys. Lett. (January 2024)

An efficient implementation of the graphics processing unit-accelerated single-step and simplified lattice Boltzmann method for irregular fluid domains

Physics of Fluids (December 2022)

25 May 2025 18:08:32

AIP Publishing

Physics of Fluids
Special Topics
Open for Submissions
Learn More
AIP Publishing

Physics of Fluids REVIEW scitation.org/journal/phf

On the lattice Boltzmann method and its application to turbulent, multiphase flows of various fluids including cryogens: A review

Cite as: Phys. Fluids 33, 041302 (2021); doi: 10.1063/5.0046938
Submitted: 8 February 2021 · Accepted: 22 March 2021 ·
Published Online: 21 April 2021

View Online Export Citation CrossMark

K. J. Petersen and J. R. Brinkerhoff[a]

AFFILIATIONS

School of Engineering, University of British Columbia–Okanagan, 1137 Alumni Ave, Kelowna, British Columbia V1V 1V7, Canada

Note: This paper is part of the Special Issue on the Lattice Boltzmann Method.
[a]Author to whom correspondence should be addressed: joshua.brinkerhoff@ubc.ca

ABSTRACT

Cryogenic fluids are used in a myriad of different applications not limited to green fuels, medical devices, spacecraft, and cryoelectronics. In this review, we elaborate on these applications and synthesize recent lattice Boltzmann methods (LBMs) including collision operators, boundary conditions, grid-refinement techniques, and multiphase models that have enabled the simulation of turbulence, thermodynamic phase change, and non-isothermal effects in a wide array of fluids, including cryogens. The LBM has reached a mature state over the last three decades and become a strong alternative to the conventional Navier–Stokes equations for simulating complex, rarefied, thermal, multiphase fluid systems. Moreover, the method's scalability boosts the efficiency of large-scale fluid flow computations on parallel clusters, including heterogeneous clusters with graphics card-based accelerators. Despite this maturity, the LBM has only recently experienced limited use in the study of cryogenic fluid systems. Therefore, it is fitting to emphasize the usefulness of the LBM for simulating computationally prohibitive, complex cryogenic flows. We expect that the method will be employed more extensively in the future owing to its simple representation of molecular interaction and consequently thermodynamic changes of state, surface tension effects, non-ideal effects, and boundary treatments, among others.

Published under license by AIP Publishing. https://doi.org/10.1063/5.0046938

25 May 2025 18:08:32

I. INTRODUCTION

In recent years, cryogenic (ultra-cold) fluids have become more prevalent in various technologies and industries. By liquefying gaseous fuels such as liquefied natural gas (LNG) and liquid hydrogen (LH_2), relatively high volumetric energy densities are achievable for use in rocket propulsion systems, nuclear magnetic resonance equipment, refrigeration, and cryoelectronics for space applications,[1] among several other applications. The high capital cost of constructing physical prototypes as well as conducting large-scale physical experiments can slow the development of new technologies. As a result, computational modeling and simulation are becoming increasingly important as a lower-cost pathway for obtaining new physical insights at a fraction of the cost of physical experimentation.

LNG and LH_2 have been proposed as alternatives to fossil fuels such as diesel and heavy fuel oil with reduced adverse environmental effects.[2,3] However, their cryogenic nature poses a unique set of physical challenges to engineering design. These include phenomena such as non-isothermal cavitation in turbomachinery, diffusion in miscible species, fuel weathering, and phase roll-over. The weathering event refers to the long-term preferential evaporation of the lightest molecules in a LNG mixture which in turn changes its composition and thermophysical properties. As a mixture weathers, it stratifies in layers of its constituent components where the upper layers become more dense from evaporation of light molecules at the free surface, and the lower layers experience superheating under the hydrostatic pressure. Eventually the increasing buoyancy between the phases results in their relocation and dangerous surges in pressure caused by evaporation of "metastable," superheated LNG.[4]

The physics of cryogenic fluids are especially important when investigating accidental spills of cryogens, which can occur in collisions between marine carriers transporting $\mathcal{O}(10^5)$ m^3 of LNG, as well as loss of mechanical integrity in flanged connections in loading arms, accidental disconnection of hoses, fracture of brittled material, and overfilling or over-pressurization of fuel storage tanks, and may lead to

Published under license by AIP Publishing

undesirable outcomes.[5] The vapor production rate following accidental spills is primarily driven by the heat transfer processes from the substrate and the environment to the cryogen. Nevertheless, the heat transfer physics involves mechanisms that are non-linear and coupled.[6] The level of complexity renders detailed modeling in numerical simulations elusive, even considering the vast amount of effort that has been invested for several decades. The majority of modeling efforts of cryogenic fluid flows have been based on continuum conservation laws especially in cavitation research.[7] The review of Yeoh and Zhang[8] gives a partial view into some of the lower-order, empirical models that are popularly employed as source-terms in the Navier–Stokes equations. Whereas the boiling physics of water are well covered, correlated, and understood in literature,[9–13] boiling of more exotic substances such as superfluids,[14] refrigerants and cryogens, boiling systems in microgravity environments,[15] and non-ideal mixtures with multiple species still demand further study. For example, the thermophysical properties of LNG, which is a zeotropic mixture, are highly dependent on its chemical composition and have significant effects on the boiling heat transfer in various boiling regimes.[16] This also applies to mixtures of liquid nitrogen (LN_2), liquid oxygen (LO_2), and liquid air.[17,18]

In space applications, the use of cryogens is absolutely essential for scientific instruments that require very low operating temperatures $\mathcal{O}(50–100)$ mK.[1] The reconnaissance "Helios" and meteorological "Meteosat"[19] satellites are equipped with infrared detectors operating at 85 K. Telecommunication satellites use superconductors to reduce size, weight, and cost, and to process radio-frequencies.[20] Gravity gradiometers operate at very low temperatures to be accurate.[21] Moreover, gaseous fuels for propulsion are most efficiently stored in their liquid form, and for future interplanetary missions, life-support systems may depend on cryogens—e.g., in fuel cells for electricity production.[22] Finally, when photo-voltaic cells cannot accommodate surges in power demand, energy can be stored in intense magnetic fields generated by superconducting magnets.[1] The required cooling power for these devices are currently provided by various mechanical coolers, e.g., Brayton, Joule–Thomson, and Stirling variants, or passive coolers such as liquid/solid cryostats and deep-space radiators.[1] Also, devices such as adiabatic demagnetization-refrigerators and dilution coolers can provide very low temperatures ($\ll 1$ K).[1] From a heat transfer perspective, current challenges in space-cryogenics include the low heat-engine isentropic efficiencies (in the range of 2%–5%), designing cryogenic heat pipes, pressure transducers, flow meters, and thermometry, predicting the effects of vibrations and micro- and zero-gravity, and more.[1]

In the above examples, the employed cryogenic fluids may involve non-isothermal conditions and the corresponding change in the fluid's thermophysical properties, miscibility of multiple liquid species, cryogenic cavitation, turbulence, compressibility, and concurrent evaporation, condensation, and freezing phase-change. Some notable challenges in the study of these phenomena with continuum conservation laws are the development of accurate and computationally inexpensive interface-tracking schemes, and the modeling of phase transitions that are naturally stochastic whereas there is not inherent stochasticity in the Navier–Stokes equations. The mesoscopic lattice Boltzmann method (LBM) has developed into a mature and efficient alternative to traditional Navier–Stokes solvers since its incipience from the lattice-gas automata formulated by Hardy *et al.*[23] and is especially known for its ability to compute multiphase flows. In comparison with Navier–Stokes solvers, LBMs represent fluid flow from a discrete, mesoscopic perspective, rather than a macroscopic continuum. There are advantages and disadvantages to both methods, but the most prominent advantage of the LBM is its superior scalability, and notable disadvantages are high memory requirements and a lack of physical interpretation in many of the discretized lattice Boltzmann equations (LBEs). The method has been used in a range of new applications in phase transitions, turbulence modeling, and micro- and nano-fluidics. The reviews of Aidun and Clausen,[24] Arumuga Perumal and Dass,[25] Chen and Doolen,[26] and Li *et al.*[27] assessed the developments in the lattice Boltzmann method for simulating rarefied multiphase flows and heat transfer. However, there is still a need for a more exhaustive synthesis of LBM works on cryogenic flows. Accordingly, our review focuses on cryogenic fluid systems broadly, as well as LBMs that can be used for the analysis of the previously mentioned effects in cryogenic flows.

This review is structured as follows: Sec. II brings an introduction to the Boltzmann equation, Sec. III presents approaches for modeling the collision between distributions of particles, and Sec. IV refers to some relevant boundary treatments. In Sec. V, techniques for adaptive mesh refinement are presented, in Sec. VI multiphase models for treating phase change and interfacial transport are presented, and high-order schemes are discussed in Sec. VII. Section VIII reviews selected cryogenic fluid systems analyzed with LBMs. Our review is concluded in Sec. X in which we suggest possible directions for future work.

II. THE BOLTZMANN EQUATION

Rarefied gas flows can be described as flows where the statistical distance between molecules following collisions, termed the mean free path (MFP), becomes significant compared to the characteristic geometric length scale of the flow.[28] In this scenario, the flow cannot be described by continuum models based on the Navier–Stokes equations which consider macroscopic properties of fluids. In assessing rarefied flows, the Knudsen number is often used to compare the MFB, λ, with the characteristic length scale, L: $Kn = \lambda/L$. At large Knudsen numbers, relatively few collisions occur and the number of molecules in a control volume is relatively small. As a result, the properties of the fluid can vary significantly. Referring to the Maxwell–Boltzmann distribution, the event that a large number of molecules will obtain velocities in the highest and lowest quantiles of the distribution inside a control volume may produce a significant perturbation in the properties of the fluid in that control volume, and thereby may initiate the creation of a new thermodynamic phase.

At high Kn, the interaction between solid substrates and molecules significantly affects the flow's evolution. As it is not feasible to resolve the motion of all particles, we instead rely on statistical mechanics to describe the average macroscopic thermophysical properties from the appropriate microscale parameters. This is where the Boltzmann equation can describe the exact dynamics of discrete particles in a flow from a particle-number-velocity distribution f,[26–29]

$$\frac{\partial f}{\partial t} + \mathbf{c} \cdot \nabla f = \Omega. \tag{1}$$

25 May 2025 18:08:32

Published under license by AIP Publishing

Herein, $\mathbf{c}$ is the particle velocity and f is the probability density function representing the proportion of particles with a particular $\mathbf{c}(\mathbf{x}, t)$ at location $\mathbf{x} = [x_\alpha, x_\beta, x_\gamma]$ and time t. The probability density function f is dependent on the time evolution of the particle following its trajectory, which is inferred through the local particle collision tensor, Ω. Ω encompasses all physical phenomena that defines its behavior in relation to the thermodynamic equilibrium state. For example, immediately after an mth particle collides with a lth particle that has a probability density $f^{(l)}$ of colliding with the mth particle, Ω changes $f^{(m)}$ by an amount $^{(m)} = \mathscr{G} - \mathscr{L}$.[28] $\mathscr{G}$ describes the gain in particle-m momentum expressed by the probability of a particle-j colliding with the mth within the ranges $[\mathbf{x}^{(m)}, \mathbf{x}^{(m)} + \delta\mathbf{x}^{(m)}]$, $[\mathbf{c}^{(m)}, \mathbf{c}^{(m)} + \delta\mathbf{c}^{(m)}]$, $[\mathbf{x}^{(l)}, \mathbf{x}^{(l)} + \delta\mathbf{x}^{(l)}]$, $[\mathbf{c}^{(l)}, \mathbf{c}^{(l)} + \delta\mathbf{c}^{(l)}]$, and $[t, t + \delta_t]$ as a function of the particle surface area, and $\mathbf{x}^{(m)}$, $\mathbf{x}^{(l)}$, $\mathbf{c}^{(m)}$, $\mathbf{c}^{(l)}$, and t. In a similar fashion, the loss term $\mathscr{L}$ describes the loss in momentum of the m-th particle. The discretized lattice Boltzmann equation (2) (LBE) can be written into a streaming process (left-hand side) and a collision process (right-hand side),

$$f_i(\mathbf{x} + \delta\mathbf{x}, t + \delta_t) - f_i(\mathbf{x}, t) = \Omega. \tag{2}$$

The collision process is correlated with an offset between the non-equilibrium and equilibrium distributions and a tensor containing characteristic relaxation coefficients, which represent the ("streaming") time between individual collisions. The solution of the equation is performed along i streaming directions—including the zeroth representing no streaming—as exemplified in Fig. 1 for a D2Q5 lattice model, and computed in a discrete manner according to the algorithm in Fig. 2.

The Hermite or Taylor expansions bridge the mesoscale to the continuum limit to achieve the Navier–Stokes equations. The macroscopic flow variables such as density, velocity, and temperature, respectively, ρ, $\mathbf{U}$, T, are correlated with the sums of the statistical particle distributions for mass and momentum (f) and energy (g), in the n total streaming directions (for double distribution functions only)—the formulation varies between LBMs

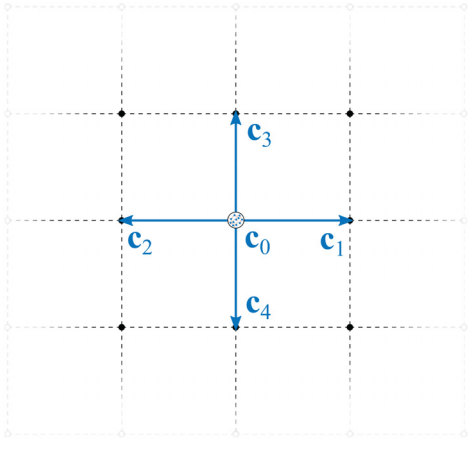

FIG. 1. Illustration of the five streaming paths (including no streaming in $\mathbf{c}_0$) in the D2Q5 lattice model.

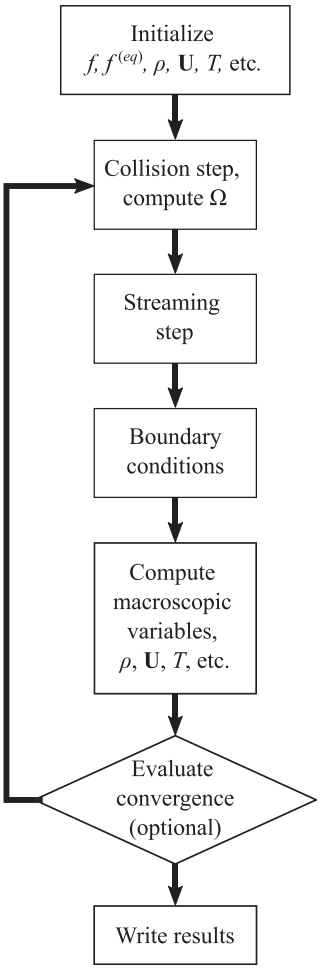

FIG. 2. General solution procedure for an LBM.

$$\rho = \sum_{i=1}^{n} f_i, \tag{3}$$

$$\rho\mathbf{U} = \sum_{i=1}^{n} f_i\mathbf{c}_i, \tag{4}$$

$$T = \sum_{i=1}^{n} g_i, \tag{5}$$

where body forces $\mathbf{F}$ are also present, the true continuum velocity is $\mathbf{U} = \mathbf{u} + \mathbf{F}\delta_t/2\rho$, where $\mathbf{u} = \frac{1}{\rho}\sum_i^n f_i\mathbf{c}_i$. The physics describing the particle interactions in multiphase flows is imposed through models using equations-of-state, free energy, interaction energies, and others. Approaches for modeling phase transitions in multiphase flows can be categorized into explicit and implicit methods.[30] In explicit methods, phase interfaces are tracked in time and space, and in implicit methods—such as the model of Shan and Chen (SC)[31]—interfaces are produced by calculating intermolecular action between adjacent

25 May 2025 18:08:32

Published under license by AIP Publishing

populations of molecules. In implicit methods, the phase transitions are spatially continuous across several lattices. This is advantageous for modeling the behavior of cryogens in environments where the temperature is not strongly dissimilar to the critical temperature requiring a high accuracy in predicting interfacial phase-change.[30]

III. COLLISION OPERATORS

Core to the lattice Boltzmann method is the way with which the thermodynamic state of a medium is altered toward one in equilibrium with a Maxwellian distribution $f^{(eq)}$ of velocities. The inequilibrated distribution f, which in the continuum limit corresponds to a temperature, changes with a rate that is dictated by the intermolecular collisions. The effects of these collisions are reflected by a collision operator Ω that relaxes the distribution function toward an equilibrium state. In the simplest form the evolution of f is represented by a single relaxation time τ in the continuous Boltzmann equation:[32]

$$\Omega_i = -\frac{1}{\tau}\left(f_i - f_i^{(eq)}\right). \tag{6}$$

However, with the collisions represented by a single relaxation time, some multi-speed lattice models with this Bhatnagar–Gross–Krook (BGK) model[33] suffers from some limitations, e.g., the Prandtl number is fixed at unity.[32] Consequently, numerous formulations of the collision operator have been proposed since Bhatnagar *et al.*,[33] not limited to multiple relaxation time (MRT) schemes and models based on entropy that also provide numerical stability at high Reynolds numbers.

To ensure stability in the simulation of turbulent cryogen flows, more sophisticated collision models with multiple relaxation times beyond the single relaxation-time BGK variant have been used. Recently, models were formulated by Mazloomi *et al.*,[34,35] and Pareschi *et al.*[36] Pareschi *et al.* presented a two-way coupled conjugate heat transfer (CHT) model applied at the fluid–solid boundary [presented as Grad's boundary condition (BC) in Sec. IV], with a two-population entropic LBM to simulate the bulk fluid kinetics. The model was validated for cases with turbulent Reynolds numbers and complex boundaries. Since the original formulation of the entropic-class LBM by Karlin *et al.*,[37] the method was considered an important milestone in the development of the LBM. It enjoyed the attention due to its unconditional stability at high Reynolds number flows in immersed complex geometries as the sub-grid physics were modeled. However, this comes at higher computational cost owing to the solution of non-linear equations for entropy. In the methods of Karlin *et al.*,[37] equilibrium population distributions were obtained by minimizing the entropy operator

$$S = \sum_{i=1}^{n}\left[f_i \ln\left(\frac{f_i}{w_i}\right)\right], \tag{7}$$

where w_i is the ith direction-dependent weight from the particular DnQm n-dimensional lattice model with m streaming directions. In order to accommodate turbulent flows, Pareschi *et al.*[36] employed the multi-relaxation Karlin–Boesch–Chikatamarla (KBC) entropic LBM[38,39] in which the double distribution functions are chosen so as to minimize S,

$$\begin{aligned} &f_i(\mathbf{x} + \mathbf{c}_i \cdot \delta_t, t + \delta_t) - f_i(\mathbf{x}, t) \\ &\quad = \omega_f\left(f_i^{(eq)} - f_i\right) + (\omega_f - \omega_{1,f})\left(f_i^{\star} - f_i^{(eq)}\right), \end{aligned} \tag{8}$$

$$\begin{aligned} &g_i(\mathbf{x} + \mathbf{c}_i \cdot \delta_t, t + \delta_t) - g_i(\mathbf{x}, t) \\ &\quad = \omega_f\left(g_i^{(eq)} - g_i\right) + (\omega_f - \omega_{1,f})\left(g_i^{\star} - g_i^{(eq)}\right). \end{aligned} \tag{9}$$

In these kinetic equations, pseudo-equilibrium distributions—denoted by "$\star$"—were adopted to allow for variable Prandtl numbers that otherwise are fixed to 1 in collision models with single relaxation times. The relaxation parameters ω_f and $\omega_{1,f}$, where subscript "f" denotes fluid (there are also parameters defined for the solid domains), allow for variable kinematic viscosity ν and thermal diffusivity α via

$$Pr = \frac{\nu}{\alpha} = \frac{(2-\omega_f)\omega_{1,f}}{(2-\omega_{1,f})\omega_f}. \tag{10}$$

The collision operators in Eqs. (8) and (9) replaced the conventional BGK collision model, which is deficient at relatively high Reynolds numbers due to numerical instabilities inducing deleterious divergence. Nevertheless, because of the simplicity and computational efficiency, the BGK collision model remains the workhorse of most LBM-implementations.[39]

Owing to the BGK popularity, the LBM was conjectured to be unsuitable for simulating high Reynolds number flows. A number of recent studies have shown this to be incorrect, as in addition to the use of the entropic LBM,[40,41] recent studies[42–46] have simulated turbulent flows with MRT collision operators—all outlined in Table I. Whereas the BGK collision model adopts a single fixed rate $1/\tau$ for f, in the MRT collision model all moments are relaxed by individual rates[42] from relaxation ($\mathbf{S}$) and transformation ($\mathbf{M}$) matrices,[47]

$$\Omega_i = -\mathbf{M}^{-1}\mathbf{S}\mathbf{M}\left(f_i - f_i^{(eq)}\right)\Delta t. \tag{11}$$

From the basic notion that the moments in an LBM—i.e., the lower-order density (zeroth), momentum (first), momentum flux (second), and those of higher order—relax toward their equilibrium states at dissimilar rates[42] brings to reason how representing the turbulence energy-cascade with a single rate can be deleterious and produce non-trivial errors. Whereas the low-order moments are inferrable from the fluid properties,[46] the higher-order moments are non-interpretable and are normally fixed at a constant value.[42] Being able to fine-tune each of the rates adaptively during runtime is paramount to eliminating numerical dispersion.

Other methods for relaxing the higher-order moments than with entropy as in the KBC model have been formulated. Li *et al.*[42] recently introduced a "measurement functional" that adjusts the higher-order moment relaxation rates on-the-fly. Other turbulence-studies using MRTs such as those of Wu *et al.*,[44] Zecevic *et al.*[46] showed good agreement with the Navier–Stokes equations from other direct numerical simulations[49,50] (DNS), in terms of turbulence-energy budgets. With more sophisticated formulations of the relaxation rates in MRT schemes and entropic extensions, stable simulations of turbulent flows are becoming a part of the repertoire of the LBM.

IV. BOUNDARY CONDITIONS

Boundary treatments define how the streaming fluid particles interact with molecules in solids. Several boundary condition (BC) models have been proposed, and are frequently published. The most commonly used BC models are standard bounce-back (SBB),[51–55] which are simple but normally achieve only first-order accuracy. The

25 May 2025 18:08:32

Published under license by AIP Publishing

TABLE I. Selected numerical experiments with the LBM of various turbulent flows since 2018. Collision models employed: entropic,[40,41] MRT,[42–46] and BGK.[48] Nomenclature: cylinder/sphere diameter D, time-averaged root mean square velocity $\bar{U}_{\text{rms}}$, Taylor microscale λ, continuous phase kinematic viscosity ν_c, friction velocity U_τ, channel height h, plate/filament/channel length l, minimum and maximum stroke ϕ, flapping frequency f, span-wise length of a wing l_w, mean wing-chord $\bar{c}$, and lid velocity U_{lid}.

References	Cases	Reynolds nos.
Morrison and Leder[40]	(a) Wall-mounted cylinder	(a) $Re_D = \frac{U_\infty D}{\nu} = 2 \times 10^2$
	(b) Sediment transport around cylinder	(b) $Re_D = 1.7 \times 10^4$
Feuchter *et al.*[41]	Wall-mounted cylinder	$Re_D = 3.2 \times 10^4$
Li *et al.*[42]	(a) Tornado	(a) 8×10^4
	(b) Falling box	(b) 10^5
	(c) Plank drop	(c) 1.4×10^5
	(d) Turbulent jet	(d) 2×10^4
Zhong and Komrakova[43]	Liq. droplet breakup	$Re_\lambda = \frac{\bar{U}_{\text{rms}}\lambda}{\nu_c} = \{56.7, 57.1, 57.1\}$
Wu *et al.*[44]	Channel flows	$Re_\tau = \frac{U_\tau}{\nu}\frac{h}{2} = (180, 395, 640)$
Xu *et al.*[45]	(a) Vertical plate	(a) $Re_l = \frac{U_\infty l}{\nu} = 126$
	(b) Stationary/oscillating cylinders	(b) $Re_D = \{100, 185\}$
	(c) Flapping foils	(c) $Re_c = \frac{U_\infty c}{\nu} A\{1, 1.1, 10\} \times 10^3$
	(d) Flexible filaments	(d) $Re_{lf} = \{200, 10^3, 7.8 \times 10^3, 9 \times 10^3\}$
	(e) Wavy wall	(e) $Re_h = 2.4 \times 10^3$
	(f) Stationary sphere	(f) $Re_D = \{1, 2.5, 3, 5\} \times 10^2$
	(g) Hovering dragonfly	(g) $Re = \frac{2(\phi_{\max} - \phi_{\min})fl_w\bar{c}}{\nu} = 2.495 \times 10^3$
Zecevic *et al.*[46]	Channel flow	$Re_l = 180$
Hegele *et al.*[48]	Cavity flow	$Re = \frac{U_{\text{lid}} l}{\nu} = 5 \times 10^4$

SBB condition infers the boundary effects by traversing particles through links crossing the solid–fluid boundary, as depicted in Fig. 3. Interpolated bounce-back (IBB) and halfway bounce-back—an SBB subclass[32]—conditions achieve up to second-order accuracy, but are difficult to implement due to a strong dependence on grid resolution.[56] Other popular BCs include immersed-boundary methods (IBM)[57–59] and non-equilibrium extrapolation schemes.[60] In addition, treatments for curved, complex boundaries[61–63] are often published and it is noted that the numerical stability of simulations—especially with turbulence—is affected by the boundary condition implementation.

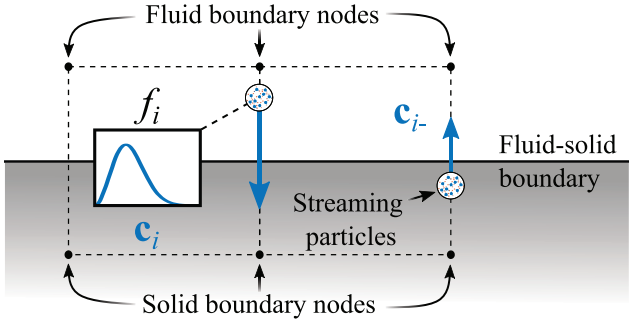

FIG. 3. Illustration of the standard bounce-back scheme. When the fluid–solid boundary is halfway between the FBN and the first fluid-immersed lattice, the method is second-order accurate.[53]

In the SBB condition, the fluid at a fluid boundary node (FBN) is bounced back with an adjustment of momentum so that the post-streaming state at a link at $\{\mathbf{x}, t + \delta_t\}$ is[24,51]

$$f_i(\mathbf{x}, t + \delta_t) = f_{i^-}(\mathbf{x}, t^+) + 2\mathbf{U}_b \cdot \frac{\rho w_i}{c_s^2} \cdot \mathbf{c}_i. \tag{12}$$

Here, i^- denotes the opposite direction of i and t^+ a time immediately post-collision but pre-streaming. $\mathbf{U}_b$ is the *in situ* boundary velocity, ρ the fluid density, w_i the weights according to the DnQm lattice definitions, c_s the speed of sound, and $\mathbf{c}_i$ the particle velocity in the ith direction. The transfer of momentum to the solid boundary $\mathcal{F}_{i^-}$ is then

$$\mathcal{F}_{i^-}(\mathbf{x}_b, t) = -2\mathbf{c}_i \left[f_{i^-}(\mathbf{x}, t^+) + \frac{\rho w_i}{c_s^2} \mathbf{U}_b \cdot \mathbf{c}_i \right]. \tag{13}$$

This momentum transfer constitutes the macroscopic pressure exerted on the wall.

Rigorous conjugate heat transfer (CHT) algorithms are particularly critical for pool boiling simulations, as the evaporation rate of the spilled cryogen is dependent on thermal conduction in the solid substrate.[64] Moreover, it is also relevant to cryogenic spill scenarios on liquid substrates, including seawater, where continuous convective heat transfer from water into the spilled cryogen may lead to solidification of the seawater as ice. A stable CHT model is essential to model such spill scenarios. Grad's boundary condition—employed for entropic LBMs by Chikatamarla *et al.*,[65] Dorschner *et al.*,[66] and Pareschi *et al.*[36]—is a stable CHT treatment useful for cases where spatial gradients in the boundary velocity and temperature are non-negligible.[36] The virtues of the scheme are a higher accuracy and broader stability

25 May 2025 18:08:32

Published under license by AIP Publishing

in contrast to the interpolated bounce-back scheme (which is already a second-order scheme). Furthermore, it can be used to model either two-fluid interfaces or solid–fluid boundaries and is suitable for high Reynolds numbers.

To illustrate Grad's boundary condition, consider the post-propagation particle distributions streaming away from the solid into the fluid depicted in Fig. 4. The particle distributions at the arbitrary lattice-proximate location $\mathbf{x}_b$ at time t are unknown due to the missing information yielded after collision with the solid–fluid boundary. In order to complete the advection process of the LBM, the "missing populations" $f_i^{\text{miss}}(\mathbf{x}_b, t)$ and $g_i^{\text{miss}}(\mathbf{x}_b, t)$ (denoted Grad's distribution) were determined by Dorschner *et al.*[66] as

$$\begin{aligned} f_i^{\text{miss}}(\mathbf{x}_b, t) &= f_i^{(eq)} + f_i^{(1)}, \\ g_i^{\text{miss}}(\mathbf{x}_b, t) &= g_i^{(eq)} + g_i^{(1)}. \end{aligned} \tag{14}$$

Grad's distribution comprises the equilibrium distributions and two first-order populations denoted with superscript "(1)." The equilibrium populations are calculated as in the work of Pareschi *et al.*,[36] where the population for the f-lattice is a function of the macroscopic velocity, density, and temperature, and for the g-lattice the equilibrium state is defined by the internal energy. The non-equilibrium population set F_i for the bulk and boundary distributions results in the moments for the boundary node with coordinate $\mathbf{x}_b$,

$$F_i = w_i \left[M_0 + \frac{\boldsymbol{M}_\alpha \boldsymbol{c}_{i,\alpha}}{T_0} + \frac{(\boldsymbol{M}_{\alpha\beta} - M_0\, \delta_{\alpha\beta}\, T_0)(\boldsymbol{c}_{i,\alpha} \cdot \boldsymbol{c}_{i,\beta} - T_0\, \delta_{\alpha\beta})}{2\, T_0^2} \right], \tag{15}$$

where M_0, $\mathbf{M}_\alpha$, and $\mathbf{M}_{\alpha\beta}$ are the zeroth-, first-, and higher-order moments (listed in Table II). These are determined from the pressure tensor $\mathbf{P}_{\alpha\beta}^{(1)}$ (16), the arbitrary high-order tensor $\mathbf{R}_{\alpha\beta}^{(1),f}$ (17), the heat flux in the fluid (convection) $q_\alpha^{(1),f}$ (18), and the heat flux in the solid (conduction) $q_\alpha^{(1),s}$ (19). The notation ∂_α is shorthand for $\partial/\partial \mathbf{x}_\alpha$.

TABLE II. The first-order moments components employed in Grad's boundary distribution (14). Reproduced with permission from Pareschi *et al.*, Phys. Rev. E **94**, 013305 (2016). Copyright 2016 American Physical Society.

Population F_i (15)	$M_0^{(1)}$	$\mathbf{M}_\alpha^{(1)}$	$\mathbf{M}_{\alpha\beta}^{(1)}$
$f_i^{(1),f}$	0	0	$\mathbf{P}_{\alpha\beta}^{(1)}$
$g_i^{(1),f}$	0	$q_\alpha^{(1),f}$	$\mathbf{R}_{\alpha\beta}^{(1),f}$
$g_i^{\star(1),s}$	0	$2\nu_\beta \mathbf{P}_{\alpha\beta}^{(1),s}$	0
$g_i^{(1),s}$	0	$q_\alpha^{(1),s}$	0

$$\mathbf{P}_{\alpha\beta}^{(1)} = \sum_{i=1}^{n} \mathbf{c}_{i,\alpha} \cdot \mathbf{c}_{i,\beta} f_i^{(1)} = -\frac{1}{\omega_f} \rho T_0 \mathbf{S}_{\alpha\beta}, \tag{16}$$

$$\mathbf{R}_{\alpha\beta}^{(1),f} = -\frac{2}{\omega_{1,f}} \rho\, T_0 \left[c_v (\mathbf{U}_\alpha \cdot \partial_\beta T + \mathbf{U}_\beta \cdot \partial_\alpha T) + \mathbf{S}_{\alpha\beta}(2T_0 + c_v T) \right], \tag{17}$$

$$q_\alpha^{(1),f} = -\frac{2}{\omega_{1,f}} \cdot \rho\, c_v\, T_0\, \boldsymbol{\partial}_\alpha\, T + 2\, \mathbf{U}_\beta \mathrm{P}_{\alpha\beta}^{(1)}, \tag{18}$$

$$q_\alpha^{(1),s} = -\frac{2}{\omega_{1,s}}\, \rho_s\, c_v^s\, T_0\, \boldsymbol{\partial}_\alpha\, T. \tag{19}$$

In order to determine the temperature field surrounding the solid–fluid interface, Pareschi *et al.*[36] computed the interface location $\mathbf{x}_I$, which is the projection of the boundary node $\mathbf{x}_b$ onto the interface, as depicted in Fig. 5, as well as the spatial gradients in Eqs. (17)–(19). At the interface, the conduction continuity applies in the wall-normal η-direction

$$-k_s \left.\frac{\partial T}{\partial \eta}\right|_{\mathbf{x}_{I,s}} = -k_f \left.\frac{\partial T}{\partial \eta}\right|_{\mathbf{x}_{I,f}}. \tag{20}$$

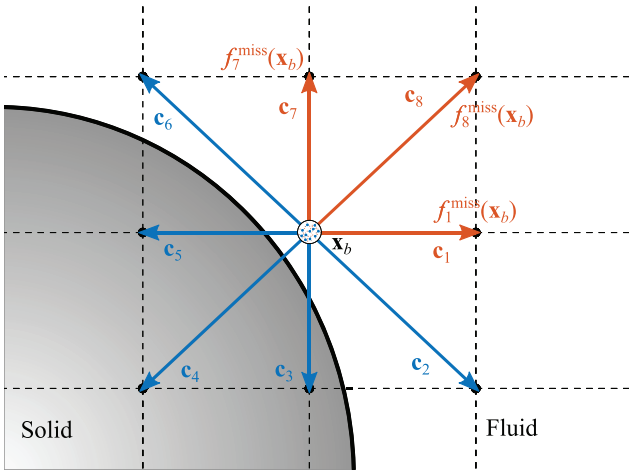

FIG. 4. Population velocities in a D2Q9 lattice where the missing populations are $f_{\{1,7,8\}}^{\text{miss}}, g_{\{1,7,8\}}^{\text{miss}}$. Reproduced with permission from Dorschner *et al.*, J. Comput. Phys. **295**, 340–354 (2015). Copyright 2015 Elsevier.

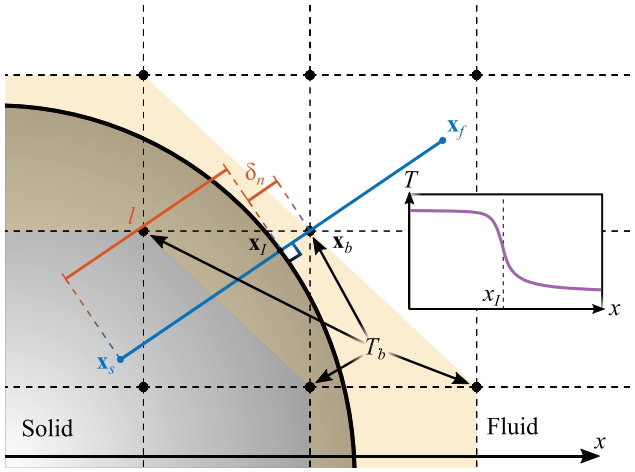

FIG. 5. Area of interest in a CHT problem where the Dirichlet and Neumann conditions do not apply. The value for $T(\mathbf{x}_I)$ in the shaded yellow region is attainable through interpolation between the target temperature at the $\mathbf{x}_b$ and an arbitrary temperature in the solid $[T(\mathbf{x}_s)]$ and fluid $[T(\mathbf{x}_f)]$. Reproduced with permission from Pareschi *et al.*, Phys. Rev. E **94**, 013305 (2016). Copyright 2016 American Physical Society.

25 May 2025 18:08:32

Published under license by AIP Publishing

Upon discretization of the above gradient, the balance below was achieved:

$$k_s \frac{T(\mathbf{x}_s) - T(\mathbf{x}_I)}{l} = k_f \frac{T(\mathbf{x}_I) - T(\mathbf{x}_f)}{l}, \tag{21}$$

$$T(\mathbf{x}_I) = \frac{k_s\, T(\mathbf{x}_s) + k_f\, T(\mathbf{x}_f)}{k_s + k_f}, \tag{22}$$

where l is defined in Fig. 5. Thus, with known fields of $T(\mathbf{x}_s)$ and $T(\mathbf{x}_f)$, $T(\mathbf{x}_I)$ can be computed. By interpolation, the target temperature at the boundary node $T(\mathbf{x}_b)$ can be calculated, and the temperature field in between nodes was calculated by linear interpolation as

$$T(\mathbf{x}_b)|_{\mathbf{x}_{b,f}} = T(\mathbf{x}_I) + \frac{\delta_\eta}{l}\left[T(\mathbf{x}_f) - T(\mathbf{x}_I)\right], \tag{23}$$

$$T(\mathbf{x}_b)|_{\mathbf{x}_{b,s}} = T(\mathbf{x}_I) + \frac{\delta_\eta}{l}\left[T(\mathbf{x}_s) - T(\mathbf{x}_I)\right]. \tag{24}$$

With the known temperature field, all the information needed to employ Grad's BC (14) is available. Pareschi *et al.*[36] used the procedure to compute the turbulent heat transfer around a wall-mounted cube immersed in air and successfully achieved a stable solution. We note that using a conjugate heat transfer BC enables the heat conduction in the solid substrate to be accounted for to accurately simulate the solid–fluid heat flux. Lately, a number of other studies[67–70] also implemented CHTs.

Cahn[71] previously showed that liquids completely wet a surface at some characteristic wetting temperature and that cooling and heating can cause a wetting transition between partial and full wetting states, i.e., the contact angle of a fluid is temperature dependent. Such a transition has also been observed in cryogens.[72–77] The wetting temperature is, however, exceptionally prone to thermal hysteresis,[77–81] and so the conjugate heat transfer and the temperature profile in a solid–fluid pair may impact the contact angle history. It has previously been remarked that the heterogeneous nucleation rate in cryogens is more susceptible to surface treatments than in water.[82] An eventual contribution from the surface topology to the interfacial tensions at a triple contact line may alter a fluid's contact angle, so it is relevant to review BCs that can account for surface energy.

Wen *et al.*[83] used a very simple, yet effective, chemical-potential based boundary scheme to evaluate the evolution of the non-ideal force [also described in Eq. (65)],

$$\mathbf{F}(\mathbf{x}) = -\rho \nabla \mu + \nabla \cdot \mathbf{P}^{(0)}_{\alpha\beta}. \tag{25}$$

Owing to its clear physical interpretation, the chemical potential is a more eloquent way of representing surface hydrophobicity and philicity, rather than through density, as is done in the pseudo-potential LBM.[31,84–86] The BC is concerned with the first layers of fluid boundary nodes (FBNs) adjacent to a solid–fluid interface and that of the neighboring solid boundary nodes (SBNs). In the FBNs, the populations still stream and collide, and distributions that rebound from the solid are approximated following the bounce-back scheme. The SBNs are treated with a Dirichlet-like condition where they are assigned a fixed chemical potential suggestive of the surface energy properties of the solid, so that the chemical potential is never computed in the SBNs. This affects the non-ideal forces—used in various equations of state (EOS)—for the nodes in proximity to the interface. The density gradient was estimated through a weighted average for the SBN density,

$$\bar{\rho}(\mathbf{x}, 0) = \frac{2}{3}\rho(\mathbf{x}, 1) + \frac{1}{6}\rho(\mathbf{x} - 1, 1) + \frac{1}{6}\rho(\mathbf{x} + 1, 1). \tag{26}$$

Figure 6 depicts the implementation of the chemical-potential BC, with the nodes in the yellow shaded region being used to compute the average.

As spilled cryogens undergo phase transitions, a triple contact line will exist that demarcates the liquid, vapor, and solid phases, illustrated in Fig. 7. The angle of the liquid/vapor interface incident to the contact line (contact angle, denoted θ) impacts the nucleation rates and heat transfer at the solid boundary as liquids with higher contact angles are less likely to fill cavities and retain vapor phases therein. Contact angle hysteresis occurs when changes in θ do not move the triple contact line; denoting angles that advance the triple contact line as θ_A and those that recede it as θ_R, the hysteresis range corresponds to $\theta_R \leq \theta \leq \theta_A$. Contact angle hysteresis has been modeled through wettability BCs in density-based contact angle schemes[86,87] and pseudo-potential-based contact angle schemes.[84,85,88] Yang *et al.*[89] implemented a contact angle hysteresis BC which established the geometric relation for the Neumann triangle depicted in Fig. 7 as

$$\tan\left(\frac{\pi}{2} - \theta\right) = \frac{\overline{AC}}{\overline{AB}} = -\frac{\dfrac{\partial \rho}{\partial z}}{\sqrt{\left(\dfrac{\partial \rho}{\partial x}\right)^2 + \left(\dfrac{\partial \rho}{\partial y}\right)^2}}. \tag{27}$$

Approximating the derivatives as difference quotients yields the density at the surface of the substrate ($z = 0$) as

$$\rho_{i,j,0} = \rho_{i,j,2} + \tan\left(\frac{\pi}{2} - \theta\right)\sqrt{(\rho_{i+1,j,1} - \rho_{i-1,j,1})^2 + (\rho_{i,j+1,1} - \rho_{i,j-1,1})^2}, \tag{28}$$

where i, j, k indices represented lattice nodes in the direction of the three coordinate unit vectors for x, y, z (not in terms of the lattice model). The hysteresis window expressed in terms of density, $\rho_R \leq \rho_{i,j,1} \leq \rho_A$, where $\rho_{i,j,1}$ pertains to the first layer nodes atop the solid surface, is obtained by evaluating Eq. (28) with θ_A, θ_R. This means that the thermophysical properties of the fluid contained inside the triple contact line can vary between ρ_R and ρ_A without changing the bubble/droplet base diameter. The formulas above present a simple way to realize the hysteresis window as Yang *et al.*[89] did in their pseudo-potential LBM. The implications of contact angle hysteresis on evaporation heat transfer in cryogens on surfaces with non-uniform

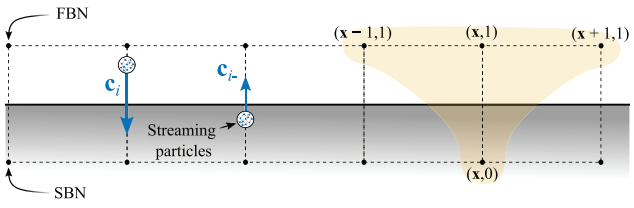

FIG. 6. Lattice structure based on the chemical-potential boundary condition of Wen *et al.*[84]

25 May 2025 18:08:32

Published under license by AIP Publishing

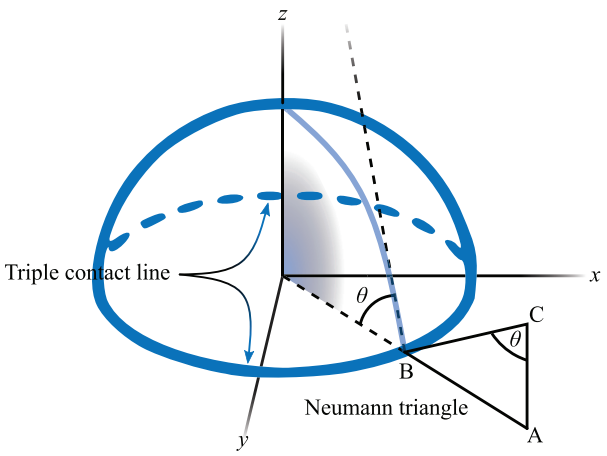

FIG. 7. Schematic of the geometric relationship which applies to the triple contact line at the periphery of a droplet or bubble, in which vapor, solid, and liquid interact. Reproduced with permission from Yang *et al.*, J. Colloid and Interface Sci. **566**, 327–337 (2020). Copyright 2020 Elsevier.

roughness, temperature, etc., may prove to be non-trivial considering that it was shown that a majority of the heat transfer takes place in and around the triple contact line and the bubble meniscus.[90] However, how strongly evaporation is affected by the hysteresis window is not clear in the literature and requires further investigation.

For thermal LBMs such as the Watari–Tsutahara–Gonella model,[91,92] the diffuse reflection boundary condition[93] proved useful for simulating rarefied flows where the slip condition applies, as well as temperature jumps, for example across shocks as investigated in the works of Traudt and Schlechtriem.[94] The BC draws inspiration from the diffuse reflection concept for gases originally proposed by Maxwell[95] and considers the solid–fluid interaction as analogous to how incident light reflects in a diffuse rather than specular manner with the strongest intensity of photons in the wall normal direction.

V. GRID-REFINEMENT TECHNIQUES

An avenue for attaining high accuracy LBM solutions at reduced computational cost is the use of multi-block (MB)[96–99] and adaptive-mesh refinement (AMR)[100–102] techniques. Ma *et al.*[103] exploited the advantages of both frameworks by developing a hybrid MB–AMR technique which combines the MB simplicity and AMR flexibility. This hybrid method belongs to the non-conformal grid approach which may result in discontinuities in the flow variables incident at the refinement interfaces. Such a framework is useful for simulating cryogenic spills on water considering that the moving surface of the water phase favors the use of AMR. In spills on solid substrates, a MB approach is useful for dividing regions of different surface energies in the lateral plane, and in the vertical plane, resolving the length scales of bubbles as they ascend, and grow/shrink in size, in the liquid column. Even though the MB–AMR technique of Ma *et al.*[103]—among others[104,105]—was purposed for neutron transport in nuclear reactors, the general algorithm can be modified to scalar/momentum transport. The indicator ϵ for the local mesh resolution was formulated in terms of the gradient of the neutron scalar flux $\nabla\Phi_s$ in block b on node s as

$$\varepsilon_{s,b} = |\nabla\Phi_s|\Delta h_b^{3/2}, \tag{29}$$

where the mesh step Δh_b varies as the MB-AMR is performed. In order to determine if a particular block should be refined or merged, standard deviation of the indicator γ_b was computed and compared to the standard deviation of the entire domain $\bar{\gamma}$, defined, respectively, as

$$\gamma_b = \sqrt{\frac{\sum_{s\in b}\varepsilon_{s,b}^2}{N_b}}, \tag{30}$$

$$\bar{\gamma} = \sqrt{\frac{\sum_b\sum_{s\in b}\varepsilon_{s,b}^2}{\sum_b N_b}}. \tag{31}$$

The overall processes of refinement and merging are depicted in Fig. 8. The lattice is initialized at the coarsest refinement level (level 1) and is subsequently resolved to higher levels (levels $2, 3, \ldots, N$). The lattice in block b is refined if $\gamma_b > \bar{\gamma}$ and lattice-nodes are merged if $\gamma_b < 0.1\bar{\gamma}$. The mesh step between finer and coarser levels is successively halved so that $\Delta x_f = \Delta x_c/2$. The simplicity in the AMR is owed to the correlation between the refinement levels by the rule that no adjacent blocks can have a resolution-level difference greater than one, which eliminates the complex tree-structured data that are inherent in conventional AMR codes.[103] In refinement "uncommon" or hanging nodes are created, and their distributions are approximated with fourth-order accuracy through a cubic interpolation scheme. During merging, a common node simply inherits the population distribution from the local node in the higher-level lattice.

Recently, several large-scale implementations of MB–AMRs have been published, revolving around simulations of lid-driven cavities, human vocal-chord flows[106] microfluidic particle separation, additive

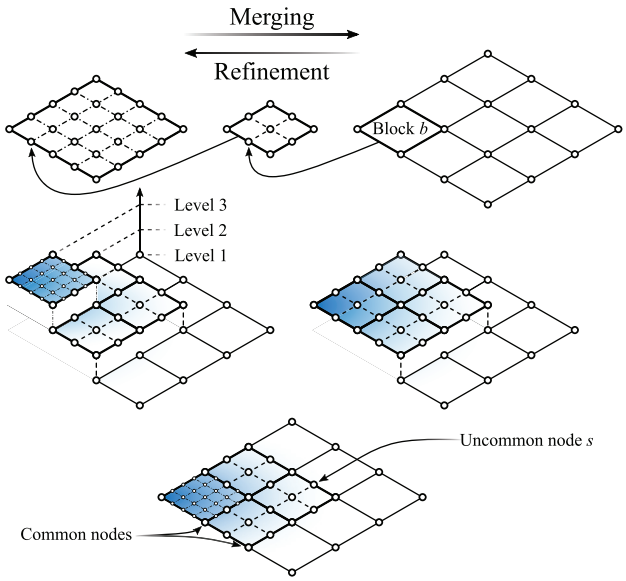

FIG. 8. Schematic of the MB-AMR technique of Ma *et al.*[103] Reproduced with permission from Ma *et al.*, Nucl. Sci. Eng. **193**, 1219–1237 (2019). Copyright 2019 Taylor & Francis.

25 May 2025 18:08:32

Published under license by AIP Publishing

manufacturing, porous flows,[107] wind farm wakes,[108] bubble breakup,[109] and Rayleigh–Taylor instabilities.[110] A focus on parallelism and acceleration using graphics processing units (GPUs) has emerged where MB-AMR schemes have been parallelized, both on homogeneous[106,108–110] and heterogeneous architectures.[107,111,112] These types of AMRs are popularly coined "para-AMRs."[110,113] Schornbaum and Rüde[106] demonstrated the peta-scale computing scalability with a MB–AMR scheme on a lattice with 13.8×10^9 nodes. On accelerators, Bauer *et al.*,[107] Hsu *et al.*,[111] and Onodera *et al.*[112] successfully partitioned block-structured AMRs with notable speed-ups and reduced communication costs via communication reduced multi-time step algorithms.[112]

VI. MULTIPHASE MODELS

Fluid systems with multiple miscible or immiscible components require special treatment. In the last decade, there were noteworthy advances in the color-gradient, pseudo-potential, free-energy, and phase-field LBMs.

A. Color-gradient LBMs

The color-gradient LBM was introduced by Gunstensen *et al.*[114] based on the two-component lattice-gas model of Rothman and Keller,[115] which applies to immiscible fluids. The color-gradient LBM applies red and blue particle distribution functions f_i^R and f_i^B, representing the velocity distributions of two fluids. The inherent disadvantages of the method are a lack of Galilean invariance, susceptibility to spurious currents, and that phase separation requires source term models. Moreover, the accuracy significantly decays at high Reynolds numbers and density ratios, which have to be compensated for with closure models. Lishchuk *et al.*[116] modeled surface tension at a two-fluid interface through a continuum surface force (CSF) equation which significantly reduced, but not completely eliminated, the occurrence of spurious currents. Latva-Kokko and Rothman[117] proposed a diffusion method for creating symmetric distributions of particles around the interface to mitigate problems with lattice-pinning, which occurs when a lattice close to an interface experiences inadequate transport of either blue or red particles, so that the interface is artificially "pinned" to the lattice. Newer variants of recoloring schemes have since then eliminated these problems. For example, Ba *et al.*[118] successfully removed spurious currents and improved accuracy at high Reynolds numbers and density ratios by decomposing the k-colored collision parameter Ω_i^k that constitutes the momentum loss or gain in the ith direction. The decomposition yields three components: a multiple-relaxation-time operator $(\Omega_i^k)^{(1)}$ that improves stability, a perturbation operator $(\Omega_i^k)^{(2)}$ that computes high-curvature interfacial forces while eliminating spurious currents, and a recoloring operator $(\Omega_i^k)^{(3)}$ for inferring a discrete immiscible fluid boundary,

$$\Omega_i^k = \left(\Omega_i^k\right)^{(3)} \cdot \left[\left(\Omega_i^k\right)^{(1)} + \left(\Omega_i^k\right)^{(2)}\right]. \tag{32}$$

The multiple-relaxation-time operator $(\Omega_i^k)^{(1)}$ in Eq. (33) projects the color-specific distribution function f_i^k from the discrete space to the moment space, i.e., the continuum so that $\mathbf{m}_i^k = \sum_j M_{ij} f_j^k$ is a matrix including stress tensor components, densities, and other thermophysical properties,

$$\left(\Omega_i^k\right)^{(1)} = \sum_j (\mathbf{M}^{-1}\mathbf{S})_{ij}\left(m_j^k - m_j^{k,(eq)}\right) + \sum_j (\mathbf{M}^{-1})_{ij} C_j^k. \tag{33}$$

$\mathbf{S}$ is a diagonal matrix related to fluid viscosity, C_j^k is a source term which recovers the Navier–Stokes equations through the Chapman–Enskog expansion, and F_s is an interfacial tension force. $f_i^{k'}$ is the post-perturbation distribution function and $f_i^{k''}$ is the post-segregation distribution function. The perturbation operator[119] $(\Omega_i^k)^{(2)}$ in Eq. (34) generates interfacial tension using a continuum surface force (CSF) model (35), such as those of Halliday *et al.*[120] and Lishchuk *et al.*,[116] through the curvature $K = -[\mathbf{I} - \mathbf{n}\cdot\mathbf{n}]\cdot\nabla\cdot\mathbf{n}$, interfacial tension σ, and the phase field function $\rho^N = (\rho^R - \rho^B)/(\rho^R + \rho^B)$,[114,121]

$$\left(\Omega_i^k\right)^{(2)} = A^k w_i\left(1 - \frac{\omega^k}{2}\right)[3(\mathbf{c}_i - \mathbf{U}) + 9(\mathbf{c}_i\cdot\mathbf{U})\mathbf{c}_i]\cdot F_s, \tag{34}$$

$$F_s = -\frac{1}{2}\sigma K \nabla\rho^N. \tag{35}$$

Employing this operator and the CSF effectively reduces the occurrence of spurious currents and the anisotropy of the interface.

The recoloring operators formulated by Latva-Kokko and Rothman,[117] defined as

$$\left(\Omega_i^R\right)^{(3)}\left(f_i'\right) \equiv f_i^{R''} = \frac{\rho^R}{\rho} f_i' + \beta w_i \frac{\rho^R\rho^B}{\rho}\cos(\varphi_i)|\mathbf{c}_i| \tag{36}$$

and

$$\left(\Omega_i^B\right)^{(3)}\left(f_i'\right) \equiv f_i^{B''} = \frac{\rho^B}{\rho} f_i' + \beta w_i \frac{\rho^B\rho^R}{\rho}\cos(\varphi_i)|\mathbf{c}_i|, \tag{37}$$

ensure efficient phase segregation and a reasonably sharp interface. ϕ_i is the angle between the color gradient $\nabla\rho^N$ and $\mathbf{c}_i$ and β is an interface-thickness parameter $\in [0, 1]$.

It is noted that even though the combined use of Eq. (34) and the CSF scheme does not accurately recover the kinematic condition, it was successfully used to predict multispecies flows in bubble coalescence,[122] droplet formation,[123] and deformation under shearing.[124]

Recently, Wen *et al.*[125] proposed a Galilean invariant 3D color-gradient LBM with improved stability for immiscible two-phase flows. The first 3D color-gradient LBM was conceived by Tölke[126] with a D3Q19 lattice. Chapman–Enskog analysis of the LBM indicated that the following error terms in k-fluid velocity ΔU_α^k were produced in the hydrodynamic momentum equations: [127]

$$\Delta U_\alpha^k = \partial_\beta\left\{\left(\tau - \frac{1}{2}\right)\left[\frac{1}{3}c^2 - \left(c_s^k\right)^2\right] \cdot\left[U_\beta^k\partial_\alpha\rho^k + U_\alpha\partial_\beta\rho^k + \partial_\gamma\left(\rho^k U_\gamma\right)\delta_{\alpha\beta}\right]\right\}, \tag{38}$$

where $c = \delta_x/\delta_t$ is the lattice speed. In fluids with equal densities, Eq. (38) will disappear, but for dissimilar densities, Galilean invariance is lost and may impair the numerical accuracy. Wen *et al.* used an improved equilibrium distribution function $f_i^{k,(eq)}$ with a MRT collision operator to eliminate the error and ensure Galilean invariance. When a circular droplet was simulated in a uniform flow field with a LBM without Galilean invariance, the droplet morphed

25 May 2025 18:08:32

Published under license by AIP Publishing

into an elliptic shape, while it retained its circular shape with Galilean invariance.[125,128,129] Another contribution is from Lee and Ahn[130] who used a combined color-gradient-LBM and smoothed-profile-method framework to simulate spinodal decompositions and wetting of solid particles in two-fluid systems.

B. Pseudo-potential LBMs

The pseudo-potential LBM, also known as the interparticle-potential model, Shan–Chen (SC), or Shan–Doolen model, is the simplest and most popular of the Boltzmann frameworks.[31,131] The primary advantage in using the pseudo-potential LBM is that it automatically resolves, tracks and develops phase separation, without interface-tracking closure algorithms. This is due to the particle–particle interaction (for single species systems) being described by a simple force equation.[131] However, Kang *et al.*,[87] Chin,[132] Kang *et al.*,[133] and Zhang *et al.*[134] have reported issues with the scheme not being exclusively immiscible and not creating sharp interfaces. This is in the nature of the SC model which is a diffuse-interface model—the density is non-discrete across tens of lattices. Given that the interfaces are not tracked, the grid resolution must be uniform, which increases the requirement for the total number of lattices to adequately resolve interfaces.[30] Moreover, the particle–particle interaction must be relatively strong to maintain an interface which may incur stability issues.[135] For a multispecies, multiphase fluid system consisting of m components, the SC lattice Boltzmann equation (LBE) is written routinely with a relaxation scheme, for the k'th species, as[32,131]

$$f_i^k(\mathbf{x}+\delta\mathbf{x}, t+\delta_t) - f_i^k(\mathbf{x}, t) = -\frac{1}{\tau^k}\left(f_i^k - f_i^{k,(eq)}\right), \tag{39}$$

where $k \in \{1, \ldots, m\}$. In order to determine the streaming process, the equilibrium population for the kth species was formulated as an arbitrary function E of the component density $\rho^k = \sum_i f_i^k$, equilibrium velocity $\mathbf{c}_i^{k,(eq)}$, and the lattice configuration; $f_i^{k,(eq)} = E_i(\rho^k, \mathbf{c}_i^{k,(eq)})$. The equilibrium velocity distribution was used for determining $f_i^{k,(eq)}$. The velocity distribution, Eq. (40), is dependent on the mixture velocity $\mathbf{U}$ defined by $\rho\mathbf{U} = \sum_k \rho^k \mathbf{U}^k = \sum_k \sum_i \mathbf{c}_i \cdot f_i^k$, where $\rho = \sum_k \rho^k$ is the mixture density:

$$\mathbf{c}_i^{k,(eq)}(\mathbf{x}) = \mathbf{U}(\mathbf{x}) + \tau^k \delta_t \frac{\mathbf{F}^k}{\rho^k}. \tag{40}$$

For m phases, $\mathcal{G}$ makes up the $m \times m$ symmetric interaction matrix $\mathbf{G}^{k-\bar{k}}$ in Eq. (42). The intensity and direction of the interaction force is inferred through $\mathcal{G}^{k-\bar{k}}$ so that the negative and positive signs create attractive and repulsive forces, respectively.

The non-monotonic force $\mathbf{F}^k$, Eq. (41)—responsible for phase-change—is inferred from the interaction between the phase k and its adjacent lattice phase $\bar{k}$ from the effective densities ρ_{eff} and $\mathcal{G}^{k-\bar{k}}$ as

$$\mathbf{F}^k(\mathbf{x}) = -\rho_{\text{eff}}^k(\mathbf{x}) \sum_{\bar{k}} \mathcal{G}^{k-\bar{k}} \sum_i \rho_{\text{eff}}^{\bar{k}}(\mathbf{x} + \mathbf{c}_i\delta_t) \cdot \mathbf{c}_i, \tag{41}$$

where Green's function $\mathcal{G}^{k-\bar{k}}$ is defined by Kwok[136] and Shan and Chen[31,131] as

$$\mathcal{G}^{k-\bar{k}} = \begin{cases} 0 & |\mathbf{x}-\mathbf{x}'| > |\delta\mathbf{x}|, \\ \mathcal{G}^{k-\bar{k}} & |\mathbf{x}-\mathbf{x}'| = |\delta\mathbf{x}|. \end{cases} \tag{42}$$

The Boltzmann equation is coupled with this interaction force to adjust the particle velocities. The added benefit of this particular method is that it is stable at high density ratios $\rho_l/\rho_v \sim 10^3$ and relatively high Reynolds numbers, as compared to other LBMs. It has been applied to many fluid dynamics problems. Green's function can be used to represent fluid-fluid interactions as well as fluid–solid interactions such as wettability.[137] Recently, Reyhanian *et al.*[138] formulated the force in terms of the Korteweg stresses to represent phase transitions and surface tension in miscible and immiscible species.

Yang *et al.*[89] recently examined droplet morphology by invoking contact angle hysteresis—that is, the difference between the minimum (receding) and maximum (advancing) contact angles of a droplet on a surface—through a modified multi-relaxation time (MRT) pseudo-potential LBM with tunable surface tension. With $\bar{f}_i = f_i - \delta_t \bar{F}_i/2$ and $\mathbf{\Lambda}_{ij} = (\mathbf{M}^{-1}\mathbf{S}\mathbf{M})_{ij}$, the relaxed LBE in the physical space is

$$\bar{f}_i(\mathbf{x}+\delta\mathbf{x}, t+\delta_t) = \bar{f}_i(\mathbf{x}, t) - \mathbf{\Lambda}_{ij}\left[\bar{f}_j - f_j^{(eq)}\right]\Big|_{(\mathbf{x},t)} + \left(\boldsymbol{\delta}_{\alpha\beta} - \frac{\mathbf{\Lambda}_{ij}}{2}\right)\bar{F}_i(\mathbf{x}, t)\delta_t, \tag{43}$$

where the forcing terms are computed as below, with the total force $\mathbf{F} = \mathbf{F}_\Psi + \mathbf{F}_g$ including the pseudo-potential interaction force $\mathbf{F}_\Psi$ and body forces $\mathbf{F}_g$ (also known as Guo's force model[32,139]). The relaxation rates in $\mathbf{\Lambda}$ are normally calculated through the thermophysical properties of the working fluid. For example, in isothermal cases such as that of Orr *et al.*,[30] the relaxation frequency was modeled through the kinematic viscosity ν,

$$\omega = \frac{2}{6\nu + 1}. \tag{44}$$

Writing the collision process from Eq. (43) to the moment space through the linear transformation matrix $\mathbf{M}$ yielded

$$\bar{\mathbf{m}}^\star = \bar{\mathbf{m}} - \mathbf{S}(\bar{\mathbf{m}} - \bar{\mathbf{m}}^{(eq)}) + \left(\boldsymbol{\delta}_{\alpha\beta} - \frac{\mathbf{S}}{2}\right)\delta_t\mathbf{F}. \tag{45}$$

Here, the superscript "$\star$" denotes the state at $(\mathbf{x}, t)$, and $\bar{\mathbf{m}} = \mathbf{M}\boldsymbol{f}$, $\bar{\mathbf{m}}^{(eq)} = \mathbf{M}\boldsymbol{f}^{(eq)}$ and $\mathbf{F} = \mathbf{M}\,\mathbf{F}$. Following the collision process, the streaming process prescribes $\bar{f}_i(\mathbf{x} + \mathbf{c}_i\delta_t, t+\delta_t) = \bar{f}_i^\star$, where $\bar{\boldsymbol{f}}^\star = \mathbf{M}^{-1}\bar{\mathbf{m}}^\star$. The flow properties in the macro perspective were then $\rho = \sum_i \bar{f}_i$ and $\rho\mathbf{U} = \sum_i \bar{f}_i\mathbf{c}_i + \frac{\delta_t\mathbf{F}}{2}$. In order to simulate advancing and receding contact angles, the collision process was adjusted to

$$\text{Eq.}(45) + \delta_t \cdot \mathbf{C}. \tag{46}$$

Yang *et al.* used the correction term $\delta_t \cdot \mathbf{C}$ for which the D3Q19 lattice model was modeled with inspiration from Li and Luo[140] as

$$\mathbf{C} = \Big[0, \frac{76}{5}s_\nu(Q_{xx}+Q_{yy}+Q_{zz}), 0, 0, 0, 0, 0, 0, 0, -s_\nu(2Q_{xx}-Q_{yy}-Q_{zz}), 0, -s_\nu(Q_{yy}-Q_{zz}), 0, s_\nu Q_{xy}, -s_\nu Q_{yz}, -s_\nu Q_{xz}, 0, 0, 0\Big]^{-1},$$

where the tensor $\mathbf{Q}$ with the surface tension adjustment parameter κ is

25 May 2025 18:08:32

Published under license by AIP Publishing

$$\mathbf{Q} = \kappa \frac{G}{2} \psi(\mathbf{x}) \sum_i w(|\mathbf{c}_i|^2)[\psi(\mathbf{x} + \mathbf{c}_i \delta_t) - \psi(\mathbf{x})]\mathbf{c}_i \cdot \mathbf{c}_i. \quad (47)$$

This reformulation of the pseudo-potential framework gave rise to simulation of advancing and receding contact angles in hysteresis windows.

The pseudo-potential LBM has become the popular choice for simulating pool boiling processes due to the natural interface treatment without the need for interface tracking algorithms. Recently Zhou *et al.*[141] used a two-population (often referred to as double-distribution function) pseudo-potential LBM similar to the one described above with the Peng–Robinson EOS to simulate the nucleate heat transfer on square micropillar surfaces,[141] and square, circular, trapezoidal and inverted trapezoidal cavities.[142] Zhou *et al.*[142] found that arranging a grid of micropillars created nucleation sites between pairs of four pillars, whereas a smooth surface at the same thermophysical state would not experience nucleation. The nucleate heat transfer reported for the cavity boiling cases is all attributed to microlayer evaporation. Other studies on pool boiling also exist,[143–145] but to the authors' knowledge, not concerning cryogenic fluids. Other authors have used the pseudo-potential model for simulating droplet dynamics,[146] and cavitation.[147–150] The study of Ezzatneshan and Vaseghnia[147] revolved around cryogens and will be elaborated in Sec. VIII.

The accuracy of the two-population pseudo-potential models in predicting heat transfer have rarely been documented. Hu *et al.*[151] provided a comprehensive evaluation of the accuracy in the most widely used thermal models for correlating the macroscopic variables, including T, to the equilibrium populations $f_i^{(eq)}$ and $g_i^{(eq)}$. These are the internal-energy-based (ITLB), temperature-based (TTLB), and simplified temperature-based (STTLB) thermal lattice Boltzmann models, respectively, defined as

$$\text{ITLB}: \quad g_i^{(eq)} = C_p \, T f_i^{(eq)}, \quad (48)$$

$$\text{TTLB}: g_i^{(eq)} = \frac{T f_i^{(eq)}}{\rho}, \quad (49)$$

$$\text{STTLB}: g_i^{(eq)} = w_i \, T(\mathbf{x}, t)\left[1 + \frac{\mathbf{c}_i \cdot \mathbf{c}^{(eq)}}{c_s^2}\right]. \quad (50)$$

Hu *et al.* compared the thermal lattice Boltzmann (LB) models to a finite-difference simulation of natural convection in a cavity and static phase change in a 1D channel. They found that the thermal LB models contained non-trivial errors. Unfortunately, no experimental validation was performed; the numerical simulations were merely compared to the numerical heat transfer model coupled with the $k - \varepsilon$ turbulence model of Barakos *et al.*[152] Thus, no clear benchmark was provided to establish the true physical errors in the simulations.

As an alternative to the pseudo-potential LBM with phase-change, Reyhanian *et al.*[138,153] recently formulated a kinetic theory that uses "peculiar" velocities (51), which comprise both the thermodynamic velocity and the velocity of a translating reference frame, in the streaming and collision processes,

$$\mathbf{v}_i = \sqrt{\frac{P}{\rho T}} \mathbf{c}_i + \mathbf{U}. \quad (51)$$

For thermal models in which not only hydrodynamic behavior is important, but other thermophysical phenomena such as phase-change are relevant, thermodynamic consistency implies that the model possesses a well-defined temperature and specific entropy across the simulated physical regimes.[154,155] Naturally, this relies on the accurate coupling and concurrent evolution of hydrodynamic and thermodynamic behavior. As a consequence, thermodynamic consistency is often associated with a correct implementation of equations of state (EOS). The kinetic theory of Reyhanian *et al.* was thermodynamically consistent and eliminated issues related to non-satisfaction of Galilean invariance and allowed for very stable simulations of compressible flows as well as phase-change processes, without the requirement of models to compensate for latent heat transfer—such as the one by Ma *et al.*[145]

C. Free-energy LBMs

Proposed by Orlandini *et al.*,[156] Swift *et al.*,[157] and Swift *et al.*,[158] the free-energy LBM is purely rooted in thermodynamics, so that the particle collision parameter is based on the free energy functional Ψ. For one component non-ideal fluids, the Helmholtz free energy Ψ, Eq. (52), is written as a function of the bulk free energy ψ, and the free energy correlated with surface tension,[32,157–159] $\psi_\kappa = \kappa/2(\nabla\rho(\mathbf{x}))^2$,

$$\Psi(\mathbf{x}) = \int \left[\psi(T(\mathbf{x}), \rho(\mathbf{x})) + \frac{\kappa}{2}(\nabla\rho(\mathbf{x}))^2\right] d\mathbf{x}. \quad (52)$$

The capillary coefficient κ gives rise to a changing energy balance and interfacial tension in areas of high density gradients near triple junctions. From the van der Waals EOS, the non-local pressure is[157]

$$p(\mathbf{x}) = \rho \frac{\delta\Psi}{\delta\rho} - \Psi = p_0 - \kappa\rho\nabla^2\rho - \frac{\kappa}{2}|\nabla\rho|^2, \quad (53)$$

where

$$p_0 = \rho \cdot \nabla\Psi(\rho) - \Psi(\mathbf{x}). \quad (54)$$

The thermodynamic pressure tensor $\tilde{\mathbf{P}}(\mathbf{x})$ is then correlated with the mixed partial derivative of the density and the surface tension as[157]

$$\tilde{\mathbf{P}}_{\alpha\beta}(\mathbf{x}) = p(\mathbf{x})\boldsymbol{\delta}_{\alpha\beta} + \kappa \frac{\partial\rho}{\partial x_\alpha}\frac{\partial\rho}{\partial x_\beta}. \quad (55)$$

It is noted that $\tilde{\mathbf{P}}_{\alpha\beta}$ excludes the shear stress tensor, so that the tensor representing the total pressure is $\mathbf{P} = \tilde{\mathbf{P}}_{\alpha\beta} + \boldsymbol{\tau}_{\alpha\beta}$. Then the LBE for the BGK collision model is[157]

$$f_i(\mathbf{x} + \mathbf{c}_i\delta_t, t + \delta_t) - f_i(\mathbf{x}, t) = -\frac{1}{\tau}\left[f_i - f_i^{(eq)}(\rho, \mathbf{c}, \nabla\rho)\right], \quad (56)$$

where $f_i^{(eq)}$ is formulated so as to be thermodynamically consistent and upon performing a Chapman–Enskog expansion, will recover the macroscopic equations in the hydrodynamic limit with insignificant error,[157]

$$\sum_i f_i^{(eq)} = \rho, \quad \sum_i f_i^{(eq)} \mathbf{c}_{\alpha,i} = \rho \mathbf{U}_\alpha, \quad \sum_i \mathbf{c}_{\alpha,i} \cdot \mathbf{c}_{\beta,i} f_i^{(eq)} = \tilde{\mathbf{P}} + \rho \mathbf{U}_\alpha \cdot \mathbf{U}_\beta. \quad (57)$$

For binary fluid systems, Swift *et al.*[158] introduced a free energy form based on two lattice populations f_i and g_i,

25 May 2025 18:08:32

Published under license by AIP Publishing

$$\Psi = \sum \left[\psi(\rho, T, \varphi) + \frac{\kappa}{2}|\nabla\rho|^2 + \frac{\kappa}{2}|\nabla\varphi|^2 \right] d\mathbf{x}, \tag{58}$$

where the bulk free energy density ψ is defined as a functional of the density and the sum of the higher order moment, $\varphi = \sum_i g_i^{(eq)}$, including the binary interaction strength G,[158]

$$\psi = \frac{RT}{2}(\rho - \varphi)\ln\left(\frac{\rho - \varphi}{2}\right) + \frac{G}{4}\rho\left(1 - \frac{\varphi^2}{\rho^2}\right) - \rho RT + \frac{RT}{2}(\rho + \varphi)\ln\left(\frac{\rho + \varphi}{2}\right). \tag{59}$$

In order to reproduce the Navier–Stokes equations the following constraints for g_i must be obeyed:[158]

$$\sum_i g_i^{(eq)} = \varphi, \quad \sum_i \mathbf{c}_i g_i^{(eq)} = \varphi\mathbf{U}, \quad \sum \mathbf{c}_i\mathbf{c}_i g_i^{(eq)} = M_i\Delta\mu\boldsymbol{\delta}_{\alpha\beta} + \varphi\mathbf{U}_\alpha \cdot \mathbf{U}_\beta. \tag{60}$$

Herein, M_i is the fluid "mobility" yet to be introduced in Eq. (70). From the free energy density defined in Eq. (59), the chemical potential between the pertinent components $\Delta\mu$ and the pressure tensor $\tilde{\mathbf{P}}_{\alpha\beta}$ are derived as[158]

$$\Delta\mu = -\frac{G\varphi}{2\rho} + \frac{RT}{2}\ln\left(\frac{1 + \varphi/\rho}{1 - \varphi/\rho}\right) - \kappa\nabla^2\varphi \tag{61}$$

and

$$\tilde{\mathbf{P}}_{\alpha\beta}(\mathbf{x}) = p(\mathbf{x})\boldsymbol{\delta}_{\alpha\beta} + \kappa\frac{\partial\rho}{\partial x_\alpha}\frac{\partial\rho}{\partial x_\beta} + \kappa\frac{\partial\varphi}{\partial x_\alpha}\frac{\partial\varphi}{\partial x_\beta}. \tag{62}$$

The non-local pressure is then determined as[158]

$$p(\mathbf{x}) = \rho RT - \kappa(\rho\nabla^2\rho + \varphi\nabla^2\varphi) - \frac{\kappa}{2}\left(|\nabla\rho|^2 + |\nabla\varphi|^2\right). \tag{63}$$

As with the original color-gradient method, the original free-energy LBM lacked Galilean invariance. However, a handful of studies have for certain DnQm lattice models mitigated the adverse effects from the variance property. Notably, Inamuro *et al.*,[128] Kalarakis *et al.*,[129] Swift *et al.*,[158] Zheng *et al.*[160,161] improved the triangular lattice Frisch, Hasslacher, and Pomeau (FHP)[162]-model and the D2Q9, D2Q5 lattice models. Similarly to Swift *et al.*, Wen *et al.*[83] recently modified a chemical-potential based free-energy LBM through manipulation of the pressure tensor $\mathbf{P}_{\alpha\beta}$. Instead of only exerting Eq. (55) on the momentum through Eq. (57), a non-ideal force was constructed and augmented by an ideal gas pressure tensor $\mathbf{P}^{(0)}_{\alpha\beta} = c_s^2\rho\cdot\boldsymbol{\delta}_{\alpha\beta}$ coupled with the Redlich–Kwong and the Peng–Robinson EOS, yielding

$$\nabla\mathbf{P}_{\alpha\beta} = \rho\nabla\mu, \tag{64}$$

$$\mathbf{F}(\mathbf{x}) = -\nabla\mathbf{P}_{\alpha\beta} + \nabla\mathbf{P}^{(0)}_{\alpha\beta} \quad \updownarrow \quad \mathbf{F}(\mathbf{x}) = -\rho\nabla\mu + \nabla\mathbf{P}^{(0)}_{\alpha\beta}. \tag{65}$$

This formulation is thermodynamically consistent and Galilean invariant,[163] with the force computed through chemical potentials. Because the pressure tensor is not computed directly via Eq. (55), as was done in previous studies,[128,129,158,160,161] computational efficiency improved and lower spurious currents were present. Zheng *et al.*,[161] Inamuro *et al.*[164] modified the model to extend the applicability to high-density ratios, while Wen *et al.* also developed a chemical potential BC to simulate the wettability of solid surfaces.

Recently, Wöhrwag *et al.*[165] proposed a thermodynamically consistent hybrid free-energy "entropic" LBM for ternary, immiscible fluids with large density ratios of the order $\mathcal{O}(10^3)$, which subsequently was extended by Bala *et al.*[166] to wetting boundaries incident at solid walls with varying geometric and forcing schemes. The title implies that the collision of particles is correlated with the production of entropy when a particular fluid tends toward a thermodynamic equilibrium state. Approaches prior to Wöhrwag *et al.*[165] were thermodynamically inconsistent,[31,167] and could not handle significant density ratios.[168,169] Moreover, the entropic LBM proposed by Wöhrwag *et al.*[165] accommodated a broad spectrum of interfacial and surface tension ratios enabling the simulation of partial wetting states in Neumann triangles in liquid lenses, through full wetting with complete fluid encapsulation. The interfacial tension in the model was flexibly tuned by simulating a liquid lens and varying the Neumann angles until the existence curves predicted by the model matched theoretical solutions. Wöhrwag *et al.*[165] included double-well potentials to model two or more fluids, whether gaseous or liquid. The potentials were analogous to those introduced in the original free-energy model proposed by Swift *et al.*[158]

A study of the optimal EOS for the entropic LBM was also carried out by Wöhrwag *et al.*[165] A Helmholtz free-energy volumetric functional Ψ was formulated that decomposed the free energy into bulk and interfacial contributions,

$$\Psi = \int \psi_B + \psi_I \, dV. \tag{66}$$

The bulk free energy ψ_B was defined as the sum of potentials for one gas and two liquids, expressed as

$$\psi_B = \frac{\lambda_1}{2}\left[\psi_{EOS}(\rho) - \psi_0\right] \quad \text{(gas)} + \underbrace{\frac{\lambda_2}{2}\cdot C_{l,1}^2(1 - C_{l,1})^2}_{\text{liquid 1}} + \underbrace{\frac{\lambda_3}{2}\cdot C_{l,2}^2(1 - C_{l,2})^2}_{\text{liquid 2}}, \tag{67}$$

where the potentials for the liquids were of the double-well form. A thorough study on the bulk free energy with various EOS was performed by Boyer and Lapuerta[170] with the Cahn–Hillard model. Their results were for three liquid potentials. Similarly to the original free-energy formulation of Swift *et al.*[158] and Swift *et al.*,[157] interfacial forces were modeled as

$$\psi_I = \frac{\kappa_1}{2}(\nabla\rho)^2 + \frac{\kappa_2}{2}(\nabla C_{l,1})^2 + \frac{\kappa_3}{2}(\nabla C_{l,2})^2, \tag{68}$$

where λ and κ were relaxation parameters, C_l the liquid concentration, and ψ_0 the reference state free energy. The free energy ψ_{EOS} was predicted by the Carnahan–Starling (CS) EOS,[135]

$$\psi_{EOS} = \rho\left[C - a\rho - \frac{8RT(-6 + b\rho)}{(-4 + b\rho)^2} + RT\log(\rho)\right], \tag{69}$$

in which C, a, and b are fluid-critical constants.

Wöhrwag *et al.*[165] noted that the Peng–Robinson and van der Waals EOS also can be implemented relatively effortlessly. Yuan and

25 May 2025 18:08:32

Published under license by AIP Publishing

Schaefer[135] evaluated existence curves for various EOS including the CS, Peng–Robinson, van der Waals, Shan–Chen, Redlich–Kwong, Redlich–Kwong–Soave and compared them to the Maxwell construction. Yuan and Schaefer[135] noted that the CS EOS is more generic as it has no free parameters, which may lead to inferior predictive accuracy for some fluids in comparison with other EOS, despite being defined from coexistence data. For cryogenic liquid oxygen, Orr *et al.*[30] reported that the CS EOS over-predicted pressure. So, the accuracy of the Shan–Chen LBM is subject to the ability of the EOS in reproducing empirical data—it is important to validate an EOS for the specific fluid to be simulated to ensure sufficient solution accuracy. The fourth-order polynomial bulk free energy from Boyer and Lapuerta[170] was used to determine the chemical potentials $\mu_\rho = \delta\Psi/\delta\rho|_{T,\phi}$, $\mu_\phi = \delta\Psi/\delta\phi|_{T,\rho}$ and the pressure tensor $\nabla P = \rho\nabla\mu_\rho + \phi\nabla\mu_\phi$. In order to solve the equations of motion at a solid–fluid boundary, the Cahn–Hillard wall-collision model (70) was employed,

$$\frac{\partial\phi_i}{\partial t} + \nabla\cdot(\phi_i\mathbf{U}) = M_i\nabla^2\mu_{\phi_i}. \tag{70}$$

The authors assumed a value for the fluid mobility M constant when it is in reality tightly coupled with the velocity field.[171] The interparticle collisions were solved routinely via the popular BGK collision operator.

D. Phase-field LBMs

Representing interfaces in ternary fluid systems is an elusive task requiring computationally intensive interface-tracking models. The most common interface theories that are used in LBM are the Cahn–Hillard [Eq. (70)] and Allen–Cahn models.[172,173] The Allen–Cahn model includes second-order derivatives which makes it more efficient, although the use of a fourth-order approximation of the diffusion term makes it susceptible to divergence.[174,175] The Cahn–Hillard model's advantage is its conservative features in comparison with the original Allen–Cahn model, although recent efforts have produced conservative versions.[176]

One of the latest phase-field LBMs was formulated by Abadi *et al.*[171] The authors extended the tracking algorithm of Geier *et al.*[177] for a two-fluid interface to ternary fluid systems by deriving the equilibrium state volume fraction $|\phi_i|^{(eq)}$ in Eq. (71) from the Euler–Lagrange (EL) differential in Eq. (72). The EL differential equation correlates the bulk free energy Φ, the capillary force term ψ, and the chemical potential in the ith phase fraction ϕ_i, which were introduced by Boyer and Lapuerta[170]

$$|\phi_i|^{(eq)} = \frac{4}{\xi}\cdot|\phi_i(1-\phi_i)|, \tag{71}$$

$$\frac{\partial\Phi}{\partial\phi_i} - \nabla\cdot\frac{\partial\psi}{\partial\phi_i} - \mu_{\phi_i} = 0. \tag{72}$$

The advection of phase i was subsequently modeled through the following conservation equation:

$$\frac{\partial\phi_i}{\partial t} + \nabla\cdot(\mathbf{U}\phi_i) = \nabla M_i\cdot\left(\nabla\phi_i - \mathbf{n}_i|\nabla\phi_i|^{(eq)} + \frac{1}{3}\sum_{i=1}^{3}\mathbf{n}_i|\nabla\phi_i|^{(eq)}\right). \tag{73}$$

The mobility of a phase M_i—a measure of the efficacy with which one phase diffuses into a neighboring phase, as a function of boundary curvature and interfacial tension—is tightly coupled to the phase-field distribution of mass, as well as momentum transfer. Significant effort was invested in formulating mobility relations.[178–181] The mobility is especially dependent on density and the phase-field, augmenting nonlinearities. Closure is achieved through a ternary formulation of the interface-tracking LBE formulated by Geier *et al.*,[177] Fakhari *et al.*,[182] with a D2Q9 lattice configuration. Moreover, hydrodynamic stability is enforced through an LBE which accommodates high density and viscosity ratios, which reduced spurious currents to below 10^{-7} lattice units. Sadeghi and Shadloo[183] used this phase-field LBM with the Cahn–Hillard interface-tracking model to simulate single and multi-mode film boiling in agreement with the Berenson[9] and Klimenko[184] correlations. In addition to this, the method has been used to simulate a wide array of problems. Ma *et al.*[185] proposed a spectral-difference phase-field LBM for incompressible two-fluid systems and used it to simulate rigid-body rotation of Zalesak's disk, layered Poiseuille flows, bubble deformation caused by shear, Rayleigh–Taylor instabilities, and bubble coalescence. Kalantarpour *et al.*[186] employed a ternary phase-field LBM to simulate static and dynamic bubble interaction at a liquid-liquid interface, Rayleigh–Taylor instabilities, as well as coalescence of a gas bubble rising in a column of water with an oil phase. Fields of bubbles in turbulent water-air pipe flows were simulated in the direct numerical simulations of Sitompul *et al.*[187] The phase-field LBM has also been accelerated to GPUs by Alpak *et al.*[188] to investigate transient binary flows in capillary tubes as well as flows in various geological formations. Moreover, the LBM is often used to simulate the convection and growth of dendritic networks of solidifying alloys.[113,189,190]

VII. HIGH-ORDER SCHEMES FOR STABLE SIMULATION OF COMPLEX FLOWS

The LBM has been criticized for its high cost in memory, inconvenient implementation of boundary conditions of higher order accuracy, and stability issues at high Reynolds numbers.[191–193] As discussed in this review, endeavors to mitigate these drawbacks were made with various numerical implementations, such as the entropic LBM that significantly improved numerical stability. Recently, stability has been vastly improved through approaches that focus on decoupling the streaming process from the pertinent lattice. However, the recovery of high-order moments implies the manipulation of complicated expansion terms that sacrifices the simplicity of the LBM. Chen *et al.*[194] contributed to the framework of simplified and highly stable lattice Boltzmann methods (SHSLBMs),[195–198] with a highly accurate, simplified lattice Boltzmann method (HSLBM). By employing Lagrange interpolation between equispaced "ghost-nodes" as seen in Fig. 9 with a streaming distance of 1/5 of the lattice spacing, the authors' HSLBM retained third-order accuracy in space while consuming less memory and computational time than the SHSLBM, while also being more stable. Moreover, a linear extrapolation scheme, also with third-order accuracy was proposed for determining populations at the boundaries. The non-equilibrium distribution functions were interpolated at the streaming nodes from the surrounding mesh points from the 2D Lagrange formulation with polynomials a_m and b_n. To distinguish from the i-streaming direction notation, the rectangular coordinate system has the dimension $\mathbf{x} = [x^{(\alpha)}, x^{(\beta)}]$ with indices m and n,

25 May 2025 18:08:32

Published under license by AIP Publishing

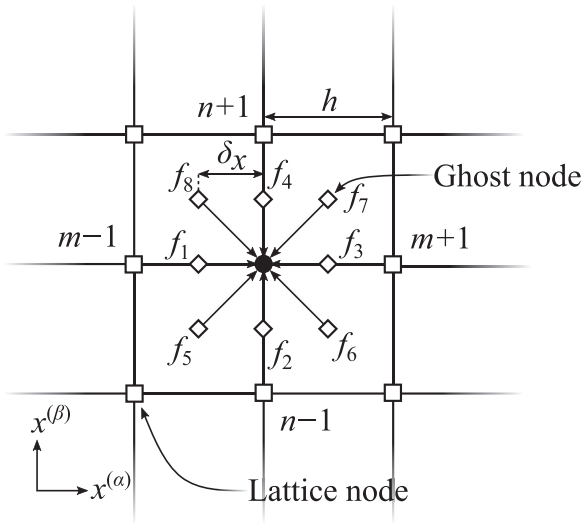

FIG. 9. HSLBM interpolation ghost nodes with a D2Q9 model. Reproduced with the permission from Chen *et al.*, Phys. Fluids **30**, 103605 (2018). Copyright 2018 AIP Publishing LLC.

$$\mathscr{L}(\mathbf{x}) = \sum_{m=1}^{M}\sum_{n=1}^{N} \mathscr{L}(\mathbf{x}(m,n)) a_m(x^{(\alpha)}) b_n(x^{(\beta)}), \tag{74}$$

$$a_m = \prod_{l=1, l\neq m}^{M} \frac{x^{(\alpha)} - x_l^{(\alpha)}}{x_m^{(\alpha)} - x_l^{(\alpha)}}, \tag{75}$$

$$b_n = \prod_{l=1, l\neq n}^{N} \frac{x^{(\beta)} - x_l^{(\beta)}}{x_n^{(\beta)} - x_l^{(\beta)}}. \tag{76}$$

A predictor–corrector scheme was adopted to obtain the macroscopic field-variables at each time step. In contrast to conventional LBMs where the distribution functions are updated in the streaming process, the HSLBM updates the macroscopic variables prior to obtaining the equilibrium distributions. This lowers the cost in virtual memory and simplifies the implementation of physical boundary conditions. The eventual numerical diffusion associated with evolution of the equilibrium distributions was recently addressed with strategies for its suppression[199] and the same method was extended to non-Newtonian fluids[200] and immersed-boundary treatments.[201]

The method has proven useful for simulating complex nanofluidic systems. Ma and Yang[202] utilized the method to simulate the natural convection from heated fins, in water–Ag–TiO_2 nanofluids. Li *et al.*[203] combined the simplified framework with the phase-field LBM to investigate multiphase ferro-hydrodynamics in ferrofluids to detail the coalescence of bubbles immersed in ferrofluid, subjected to a magnetic field. Other studies similarly investigated various configurations of ferrofluid flow problems.[204,205] It has also been formulated in terms of the finite-volume method to compute various laminar and turbulent flows.[206,207]

VIII. LBM APPLICATIONS IN CRYOGENIC FLUID SYSTEMS

This section highlights applications of the LBM to cryogenic fluid systems. The studies that have used LBMs to simulate cryogenic phase-change, summarized in Table III, are few despite the success with which LBM has been applied to other fluids. In the earlier days of the LBM maturity, Tatsumi and Nishijima[14] used the color-gradient LBM to investigate the stability of superconductivity in a wire submerged in liquid Helium (LHe_2). In more recent years, Orr *et al.*[30] reported their development of a pseudo-potential LBM for spacecraft propellant slosh simulation in microgravity environments.

In space, low Bond numbers $Bo = (\rho g L_c^2/\sigma)$ are useful for characterizing the hydrodynamic behavior of multiphase cryogenic flows—such as the oxidizer liquid oxygen (LO_2) simulated by Orr *et al.*[30]—due to the low gravitational acceleration relative to capillary forces. It was crucial to be able to alter gravitational effects, so they incorporate body forces into the LBE following the exact difference method (EDM) of Kupershtokh.[213] This method applies body forces simultaneously to the advection step and the equilibrium population where the subsequent shift in velocity due to the forcing is computed as $\Delta\mathbf{U} = \bar{\boldsymbol{\mathcal{F}}}/\rho$, where $\bar{\boldsymbol{\mathcal{F}}}$ is the momentum density, which equates to g if the gravitational field is uniform. The lattice velocity distributions are shifted to a modified velocity $\mathbf{U}^{\star}$ which is subsequently used to compute the collision process. The authors reported that the equilibrium populations must be updated at least twice during collision. The $(n+1)$-th time step was equated to the below, where (pc) is the post-collision state:

$$f[n+1] = (\mathbf{I} - \mathbf{M}^{-1}\mathbf{S}\mathbf{M}) \times \left(f^{(pc)}[n] - f^{(eq)}(\mathbf{x}, \mathbf{U}, \rho)\right) + f^{(eq)}(\mathbf{x}, \mathbf{U}^{\star}, \rho). \tag{77}$$

With the discretized LBE $f_i(\mathbf{x}+\delta\mathbf{x}, t+\delta_t) = f_i(\mathbf{x}, t) - \boldsymbol{\Lambda}[f_i(\mathbf{x}, t) - f_i^{(eq)}(\mathbf{x}, \mathbf{U}, \rho)]$, the collision matrix $\boldsymbol{\Lambda}$ expands to

$$\boldsymbol{\Lambda}_{\alpha\beta} = \boldsymbol{\Lambda}_0 + \omega_{\alpha\beta}\Delta\boldsymbol{\Lambda}_{\alpha\beta} = \mathbf{M}^{-1}(\mathbf{S}_0 + \Delta\mathbf{S}_{\alpha\beta})\mathbf{M}, \tag{78}$$

where $\mathbf{S}_0$ is the hydrodynamic part of the relaxation matrix. The matrix $\Delta\boldsymbol{\Lambda}_{\alpha\beta}$ only relaxed the diagonal and off-diagonal entries of the pressure tensor $\mathbf{P}_{\alpha\alpha}$ and $\mathbf{P}_{\alpha\beta}$, respectively. With $\Delta f[n] = f^{(pc)}[n] - f^{(eq)}(\mathbf{x}, \mathbf{U}^{\star}, \rho)$, the collision equation for the MRT scheme with body forcing is

$$f[n+1] = (\mathbf{I} - \boldsymbol{\Lambda}_0)\Delta f[n] + f^{(eq)}(\mathbf{x}, \mathbf{U}^{\star}, \rho) - \omega_{\alpha\beta}\Delta\boldsymbol{\Lambda}_{\alpha\beta}\Delta f[n]. \tag{79}$$

Crucial to the simulation of spacecraft dynamics is the total force acting on the entire fluid domain, which was computed as the difference between body forces and internal forces (in terms of momentum density),

$$\bar{\boldsymbol{\mathcal{F}}}_d[n] = \sum_{\alpha\beta} \bar{\boldsymbol{\mathcal{F}}}_{\alpha\beta} - \left(\sum_{\alpha\beta} \rho_{\alpha\beta} U_{\alpha\beta}[n] - \sum_{\alpha\beta} \rho_{\alpha\beta} U_{\alpha\beta}[n-1]\right). \tag{80}$$

Orr *et al.*[30] used the above approach to compute the lateral sloshing of LO_2 in an asymmetrical tank with a gravitational field of $g = 0.001 g_0$ at 15° in relation to the axial direction. Their 2D solution at $t = 9.8$ s is depicted in Fig. 10, which shows the velocity field in lattice units. For spacecraft dynamics in microgravity environments, convection caused by gradients in interfacial tension is characterized through the Bond number, $Bo = \rho g L_c^2/\sigma$. The primary mode oscillated with a frequency of $\mathcal{O}(10^{-2})$ Hz with a modest lateral force of $\mathcal{O}(10^{-4})$ N. The simulation showed strong advective patterns in the

25 May 2025 18:08:32

Published under license by AIP Publishing

TABLE III. Overview of published works on cryogenic fluids using LBMs: (a)—Tatsumi and Nishijima (2003),[14] (b)—Izumi *et al.* (2004),[208] (c)—Imre *et al.* (2008),[209] (d)—Orr *et al.* (2015),[30] (e)—Traudt and Schlechtriem (2019),[94] and (f)—Ezzatneshan and Vaseghnia (2020).[147]

Study	LBM	Cases	Conditions
(a)	Color gradient	Natural convection around superconducting wire	Subcooled, LHe_2, thermal response, and convective stability to varying transport currents, dynamic viscosity $\mu = 5 \times 10^{-6}$ Pa s
(b)	Pseudo-potential	Heterogeneous nucleation	Continuation of "(a)" with phase transition
(c)	Pseudo-potential	Spinodal estimation	Lennard–Jones Argon at 128 K, liquid film in vapor, gravitation-free, accompanied by molecular dynamics simulations
(d)	Pseudo-potential	Varying wetting (i)	(i): LO_2, corner geometry, negative (hydrophobic), neutral, and positive (hydrophilic) wall interaction potentials, contact angle $\theta < \pi/2$
		Lateral sloshing in tank, frequency analysis (ii)	(ii): LO_2, surface tension $\sigma = 0.0122$ N/m, Bond/Eötvös number $Bo = \Delta\rho g L^2/\sigma \sim 20$, acc. $g = 0.001 \cdot g_0$
(e)	Finite-difference, multi-speed	Lid-driven cavity (i)	(i) Gaseous nitrogen at 114 K and 0.306 MPa, laminar, incompressible flow, $Re < 5000$, ideal-gas model
		Riemann shock tube (ii)	(ii) Supercritical/gaseous oxygen, $\rho_{t=0} \in [43.6, 170](\mathrm{kg/m^3})$, $T_{t=0} \in [139, 170]$ (K), $Ma \in [1.118, 1.139]$, ideal-gas model
		Saturated film boiling (iii)	(iii): LO 2, $T_{t=0} = T_{\mathrm{sat}} = 139$ K, $\rho = 723\,\mathrm{kg/m^3}$, 1.2 MPa, $\Delta T \in [5, 62]$
(f)	Pseudo-potential	Validation study (i)	(i): H_2O , LN_2, LH_2 droplets suspended in vapor, verification with Laplace law and the Maxwell construction, validation from NIST.[210]
		Heterogeneous cavitation-bubble nucleation (ii)	(ii): H_2O, LN_2, LH_2, $\rho_l/\rho_v \in [13, 112]$, phase transition inception with the energy-barrier equation,[211] verification from the Rayleigh–Plesset equation[212]
		Cav.-bubble collapse near solid surface (iii)	(iii): H_2O, LN_2, LH_2, collapse time sensitivity to varying bubble-to-wall distance and contact angle $\theta = \{30°, 90°, 150°\}$

vapor phase in the form of rotational structures emanating from the triple junctions at the tank walls. The interface behavior at the triple junctions suggests that the wettability of the wall produces an apparent attractive effect at the pertaining low Bond number of the problem.

Traudt and Schlechtriem[94] used a van der Waals-based finite-difference LBM to simulate transient two-phase flow of cryogenic propellants in rocket engine feed systems, including test cases on single LO_2 bubble evaporation and the Riemann shock problem. Their model showed the capability to resolve shocks and supersonic flow, which are also relevant to modeling the gas dynamics involved in rapid phase transitions that may occur during high ΔT film boiling. In the design of rocket engines and their propellant feeding systems, the complexity of valve configurations and timing upon startup incur high costs in prototyping, as the integrity of the engine is highly prone to damage from the timing of said valves. The fuel and oxidizer are most often cryogenic and cavitate when the valves open and also experience heterogeneous nucleation when contacting the solid engine parts. Moreover, after cooling the rocket nozzle and being pressurized in turbopumps, the cryogens may become supercritical. Thus, numerical methods for simulating the transient startup processes are required to be stable at high Reynolds numbers, compressible, sub- and supercritical multiphase flows of non-ideal fluids, in complex geometries.

Traudt and Schlechtriem[94] used the multi-speed model of Watari and Tsutahara[91] which has proven to be accurate for supersonic flow simulations,[214] with an extension for simulating non-ideal van der Waals fluids.[92] The real-gas model of Gonnella *et al.*[92] implemented a force term similar to the pseudo-potential LBM that emulates the interaction forces between molecules to simulate phase transitions and continuous density gradients across interfaces. Since the lattice speeds are lattice-speed independent, a finite difference discretization was used with a van-Leer limiter in the flux $\ddot{F}$ at the halfway distance $j \pm 1/2$ to the neighboring node j,

$$f_i(n+1) = f_i(n) - \frac{c_k \delta_t}{w_i \delta_x}\left[\ddot{F}_i j + 1/2 - \ddot{F}_i j - 1/2\right]_{(n)} - \frac{\delta_t}{\tau}\left[f_i(n) - f_i^{(eq)}\right]_{(n)} - \delta_t \cdot F_i, \tag{81}$$

where

$$\ddot{F}_i j + 1/2 = f_i + \frac{1}{2}\left(1 - \frac{c_k \delta_t}{w_i \delta_x}\right)\left[f_i^{j+1} - f_i\right]_{(n)} \tilde{\Psi}(\Theta), \tag{82}$$

and Θ_i^j is a smoothness function and $\tilde{\Psi}$ is a flux delimiter,

25 May 2025 18:08:32

Published under license by AIP Publishing

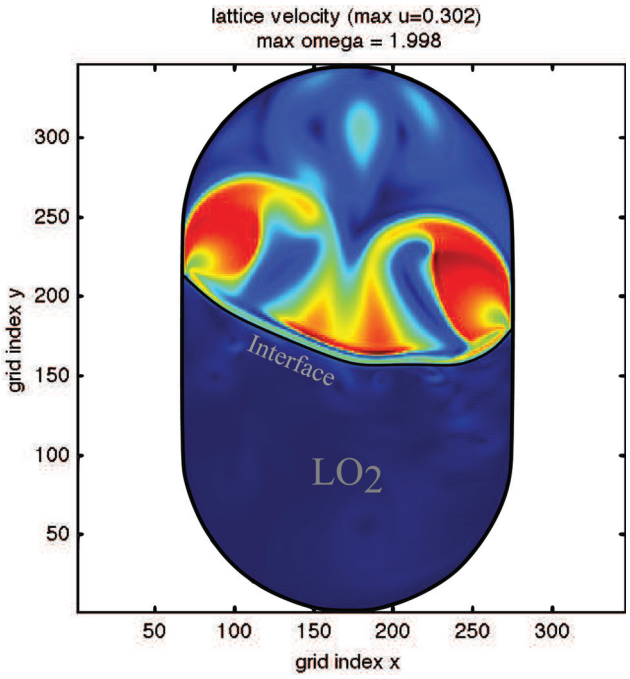

FIG. 10. Instantaneous velocity contour of LO_2 propellant undergoing lateral sloshing in a tank. Solution from an isothermal simulation with the pseudo-potential method. Reproduced with the permission from Orr *et al.*, in American Astronautical Society (AAS) Guidance, Navigation, and Control Conference (National Aeronautics and Space Administration, Breckenridge, CO, USA, 2015).[30] Copyright 2015 National Aeronautics and Space Administration.

$$\Theta_i^j = \frac{f_i^j - f_i^{j-1}}{f_i^{j+1} - f_i^j}, \tag{83}$$

$$\tilde{\Psi} = \begin{cases} 0 & \Theta_i^j \le 0 \\ \dfrac{2\Theta_i^j}{1+\Theta_i^j} & \Theta_i^j > 0. \end{cases} \tag{84}$$

The multi-speed model produced no error through the Chapman–Enskog expansion and improved stability in multiphase, compressible flows. The van der Waals EOS contains derivatives that Traudt and Schlechtriem[94] computed with a fourth-order accuracy through a nine-point discretization. The authors' simulations comprised a Riemann shock problem with LO_2. In comparison with the analytical solution of Wagner,[215] predictions for the velocities, pressures, temperatures, and densities for four different simulations incurred <1% error. Traudt and Schlechtriem[94] also simulated the film boiling of LO_2 with good agreement with experiments.

The comparative study of Peng *et al.*[216] found that of the velocity shifting method (VSM), exact difference method (EDM) and Guo's force schemes, the VSM and EDM allowed for the highest density ratios. Thus, Ezzatneshan and Vaseghnia[147] employed the VSM and EDM in a pseudo-potential LBM for studying the nucleation and collapse of cavitation bubbles in water, LN_2, and LH_2. In the VSM, the hydrodynamic velocity is shifted by the sum of the pertinent body forces (e.g., interaction, gravitational, fluid–solid) **F** so that the velocity used in the equilibrium distribution is

$$\mathbf{U}^{(eq)} = \mathbf{U} + \frac{\tau \mathbf{F}}{\rho}, \tag{85}$$

and the real velocity field is redefined as

$$\tilde{\mathbf{U}} = \mathbf{U} + \frac{\mathbf{F}\delta_t}{2\rho}. \tag{86}$$

In the EDM, the body forces are directly added to the RHS of the LBE,

$$f_i(\mathbf{x} + \mathbf{c}_i\delta_t, t + \delta_t) - f_i(\mathbf{x}, t) = -\frac{\delta_t}{\tau}\left[f_i(\mathbf{x}, t) - f_i^{(eq)}(\rho, \mathbf{U})\right] + f_i^{(eq)}(\rho, \mathbf{U}, \Delta\mathbf{U}) - f_i^{(eq)}(\rho, \mathbf{U}), \tag{87}$$

where $\Delta\mathbf{U} = \mathbf{F}\delta_t/\rho$. Ezzatneshan and Vaseghnia conducted a sensitivity analysis of the bubble nucleation/collapse dynamics with varying vapor-to-liquid pressure differences $\Delta P = P_l - P_v$ via the "energy-barrier equation"

$$\Delta E = 4\pi R^2\sigma + \frac{4}{3}\pi R^3 \Delta P, \tag{88}$$

which relates the total system energy to the cavity radius R and the surface tension σ. The inequality of this equation leads to phase transition, but the equality preserves any liquid-vapor pair in an equilibrium state where a critical pressure difference $\Delta P_c = -\sigma/R$ (the Laplace law) is unique for a fluid—i.e., $\Delta P_c = \{-0.009\,028\,5, -0.006\,335\,9, -0.009\,028\,5\}$ (lattice-units) for H_2O, LN_2, and LH_2, respectively.[147] The authors were able to verify the growth dynamics from the Rayleigh–Plesset equation[212] and investigated the nucleation of a cavity in a liquid filled with microbubbles, as well as the collapse of a cavity near a solid wall with varying wettability and wall-to-cavity distance. The authors found that the collapse of the water cavity, in comparison with the cryogens, was more aggressive (as indicated in Fig. 11), in agreement with the experiments of Dular and

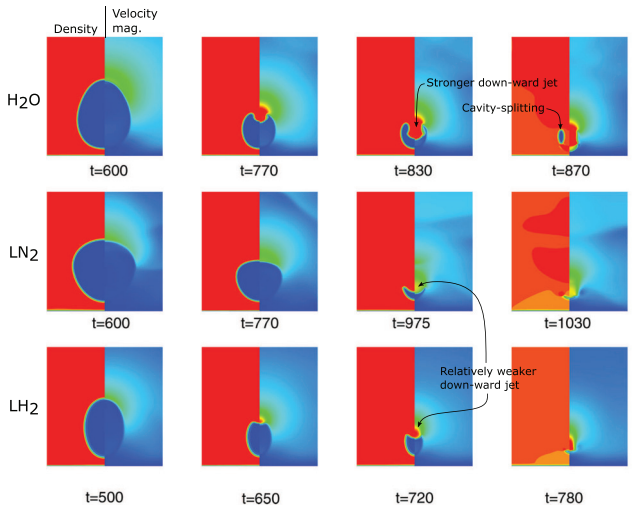

FIG. 11. Collapse of H_2O, LN_2, and LH_2 cavities near a solid wall by Ezzatneshan and Vaseghnia.[147] Reproduced with permission from Ezzatneshan and Vaseghnia, Phys. Rev. E **102**, 053309 (2020). Copyright 2020 American Physical Society.

25 May 2025 18:08:32

Published under license by AIP Publishing

Petkovšek.[217] The distinct collapsing behavior was owed to the implementation of the acentric factor in the authors LBM which is a measure of the molecular structure and polarity in a fluid, where a low acentricity is associated with spherical molecules with low polarity.[218]

A stable liquid is bounded by its equilibrium curve between its freezing and boiling points, but outside of this in the metastable region the liquid will become unstable and prefer a new thermodynamic state. However, beyond the equilibrium with either superheating or subcooling substances can exist in their liquid state under certain conditions—i.e., if no impurities exist and the system is not disturbed by external forces.[219] However, the metastable region is similarly bounded by stability limits in either of the directions of superheating and subcooling, beyond which vapors and liquids cannot exist.[209] Such a limit is termed a "spinodal" and these are impossible to determine experimentally[209]—a full elimination of impurities and disturbances in a given substance is impractical to achieve. Accordingly, Imre *et al.*[209] simulated a liquid film surrounded by vapor in a zero-gravity environment, with a pseudo-potential LBM (and a molecular-dynamics simulation). They found that the employed equation of state[31] in the LBM—extended deep into the metastable extremes—was able to reproduce the liquid spinodal for argon, derived from experimental results for interfacial thickness and surface tension. The authors' simulations are useful for further development of EOS applicable to metastable systems.

Modeling accidental spills of cryogenic fluids on water is relevant to shipping of LNG and its use as a marine fuel. Accurate models of cryogenic spills require elucidating the heat transfer characteristics of the ice formed in water following contact with the cryogenic LNG, as well as a better understanding of how water turbulence affects the freezing rate and overall heat transfer between the two fluids. Recently, Li *et al.*[220] proposed a pseudo-potential LBM with a concurrent evaporation, condensation, and freezing phase-change model based on enthalpy. The authors employed two populations for momentum and energy, Eqs. (89) and (92), to resolve the velocity, pressure, and temperature fields,

$$f_i(n+1) - f_i(n) = -\frac{1-B}{\tau_f}\left[f_i - f_i^{(eq)}\right] + B\Omega_i^s + (1-B)\Delta f_i. \quad (89)$$

$\Omega_i^s = f_{i^-} - f_i + f_i^{(eq)}(\rho, \mathbf{U}_s), -f_i^{(eq)}(\rho, \mathbf{U})$ is a bounce-back collision term for the non-equilibrium part of f with $\mathbf{U}_s$ being the velocity of the solid. The f-population was weighted by B which relaxes the collision process as a function of the relaxation time τ_f and the solid volume fraction f_s,

$$B = \frac{f_s(\tau_f - 1/2)}{1/2 - f_s + \tau_f}. \quad (90)$$

The solid volume fraction is unity for an iced phase and zero for liquid, and $0 < f_s < 1$ for multiple phases including vapor, and was determined based on enthalpy,[137]

$$f_s = \begin{cases} 0 & H > H_l \\ \dfrac{H - H_s}{H_l - H_s} & H_s < H < H_l \\ 1 & H < H_s. \end{cases} \quad (91)$$

The population corresponding to energy is a function of two source terms ϕ_{vl} and ϕ_{ls}

$$g_i(n+1) - g_i(n) = -\frac{1}{\tau_T}\left[g_i - g_i^{(eq)}\right] + \delta_t w_i(\phi_{vl} + \phi_{ls}). \quad (92)$$

The generic algorithm computed the freezing phase change by computing ϕ_{vl} and ϕ_{ls} prior to the collision step, and enthalpy and f_s after computing the macroscopic variables. In terms of Fourier number, $Fo = \alpha_s t/l_0^2$, Li *et al.*[220] simulated a cryogenic spot with water vapor undergoing condensation and freezing phase change.

The phase morphology predicted by Li *et al.*[220] for a droplet solidifying on a vertical substrate is depicted in Fig. 12. In agreement with Yang *et al.*,[89] Li *et al.*[220] noted that surface wettability affects the morphology of liquid droplets but not the growth of ice under concurrent evaporation, condensation, and freezing phase-change. The wettability was inferred through the body forces $\mathbf{F} = \mathbf{F}_\Psi + \mathbf{F}_s + \mathbf{F}_g$ with $\mathbf{F}_s$ representing fluid–solid interaction. Preceding this work, Sun *et al.*[137] developed a LBM for modeling the freezing phase-change heat transfer within a droplet as well as surface frost formation on a horizontal surface from air humidity. To resolve the frost layer, they adopted porous media permeability theory so that the fluid streams according to $f_i'(\mathbf{x} + \delta\mathbf{x}, t + \delta_t) = f_i(\mathbf{x}, t)$ when $f_s = 0$, the populations remained stationary when $f_s = 1$, and if $0 < f_s < 1$ the populations contained a solid–fluid mixture and only a fraction of f_i streams with a modified streaming equation,

$$f_i'(\mathbf{x} + \delta\mathbf{x}, t + \delta_t) = (1 - f_s)f_i(\mathbf{x}, t) + f_s f_i(\mathbf{x} + \delta\mathbf{x}). \quad (93)$$

In addition, Zhao *et al.*[221] simulated the impact dynamics of a droplet on freezing surfaces. The importance of concurrent evaporation, condensation, and freezing phase-change in cryogenic spills is

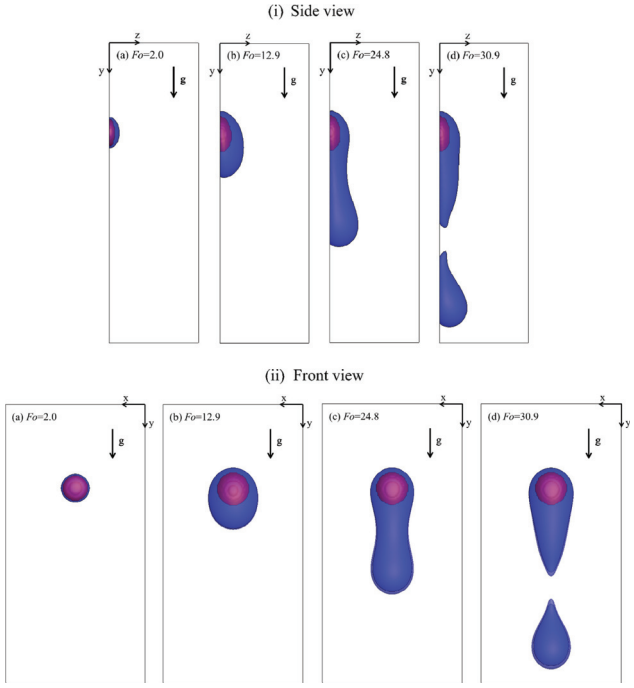

FIG. 12. Freezing droplet morphology as reported in the paper by Li *et al.*[220] The ice phase is purple and the liquid phase blue. Reproduced with permission from Li *et al.*, Int. J. Heat Mass Transfer **114**, 628–639 (2017). Copyright 2017 Elsevier.

25 May 2025 18:08:32

Published under license by AIP Publishing

exemplified in the fact that the cryogen comes in contact with water in ocean spills in which an ice film will interact with both the ambient humid air and water phases. Furthermore, the subsequent dispersion of the cold vapor triggers the condensation of the unsaturated vapor in the air.

IX. DISCUSSION

Throughout this paper, we have presented lattice Boltzmann methods relevant to many fluid and flow configurations, despite cryogens being our main area of research. The limited number of studies discussed in Sec. VIII shows that application of LBMs to cryogens is still in its infancy, and requires further development. In particular, the authors' aim is to conduct massively parallel simulations of accidental spills of cryogens (especially liquefied natural gas and hydrogen) on solid substrates as well as on water to elucidate the fundamental nature of the pertinent fluid dynamics as well as inform our industrial partners and their work with storage and transport of LNG and LH_2.

There are several challenges in formulating the relevant numerics for the physics that constitute this problem. The interaction between nucleation sites in the nucleate boiling regime on solid substrates will require the simulation of clusters of sites. This contrasts the studies reviewed herein, that only considered the evolution of bubbles from a single nucleation site. Furthermore, wetting transitions have been observed in cryogens,[72–77] meaning that they are susceptible to thermal hysteresis. As the ability for a fluid to nucleate is proportional to its ability to spread on a solid surface, knowledge of the contact angle dynamics is important to accurately predict nucleation rates. In contrast to water which is polar, cryogens exhibit weak self-mutual molecular interactions that can be represented by van der Waals forces.[222] In order to infer a rigorous thermal dependence, future research can investigate the formulation of explicit temperature dependence in, e.g., the pseudo-potential LBM. The contact angle of cryogens, which virtually is zero,[82] results in non-isothermal phase-change and thereby a non-trivial dependence on a thermal condition in the molecular interaction potentials. A parametric investigation of contact angle hysteresis in cryogens does not exist on the basis of the presently reviewed content, although analytical approximations do exist.[223,224] Additionally, as cryogens are especially sensitive to surface treatments,[82] an elucidation of their effects on the contact angle will also be valuable for finding methods for controlling the onset of boiling and critical heat flux, which is relevant to minimizing boiloff in storage applications.

Successful simulations of cryogenic spills will include concurrent turbulence, freezing and boiling phase change, contact angle hysteresis, various free-surface perturbations, Rayleigh–Taylor instabilities and splashing, and conjugate solid–fluid heat transfer. As exemplified so far, each of these fundamental phenomena have been simulated separately, and the associated publications provide a road-map for the design of more complicated multi-physics simulations of realistic spill scenarios. To our knowledge, no investigations have attempted to encompass all of these simultaneously in a single framework. We expect that this will constitute an enormous challenge. Given the span of scales in cryogenic spill problems both in terms of the turbulence cascade and the evolution of embryonic nuclei to detached, fully developed bubbles, direct numerical simulations will be appropriate for our planned work. The associated computational demand will necessitate high-performance computing resources. The presented para-AMRs (Sec. V) and methodologies for GPU-acceleration[42,44,107,111,112] may prove beneficial.

This review can also pave the way for investigations of other problems, where the above-mentioned phenomena also occur. The majority of the reviewed LBMs revolved around immiscible species. LNG, which is a multi-component mixture, experiences species stratification over time, potentially resulting in adverse roll-over phenomena. Accurate modeling of these requires LBM frameworks with the capability of simulating ternary mixtures with cross-diffusing species, which requires more development. Recently, a couple of studies have developed miscible extensions in the phase-field LBM[225] and through forcing terms,[226] for which the latter can be extended to all of the LBMs reported herein. In diffuse interfaces where diffusion is so slow that large interfacial concentration gradients exist for extended durations, Korteweg stresses, or "effective interfacial tension" arise,[227] which can drive viscous fingering instabilities.[228] Elucidating if this can trigger roll-over in LNG is another avenue for research. In favor of this, the Korteweg stress has recently been incorporated in a kinetic theory.[138]

In space-craft propulsion—specifically compressors—cryogenic fluids can reach their supercritical states. In such applications equations-of-state that can cover the sub- and supercritical regimes in cryogens are important. A further review of equations of state that can cover this range and are applicable to cryogens would be valuable. In turbomachinery used in pumping applications for cryogen storage and transport, cryogens can undergo cavitation. Previous studies have investigated cavitation[147–150] as well as compressible flows of cryogens[94] and other fluids.[138]

In addition, the review has included several LBMs with applications of other fluid systems as a by-product, not limited to nanofluids, porous flows, biological flows, neutron transport, among others, that can hopefully inspire readers studying other topics than cryogenic fluids.

X. CONCLUSION AND FUTURE WORK

We have identified some key applications in which cryogenic fluids such as liquefied natural gas (LNG), hydrogen (LH_2), and helium (LHe_2), are used—propulsion systems in trucking, marine carriers, and spacecraft, as well as medical devices and scientific equipment in spacecraft, among others. Ultracold LNG and LH_2 have much higher densities compared to their gaseous states making them more cost-efficient during marine transport. However, in their cryogenic state, their interaction with standard-state conditions is associated with non-isothermal phase-change mechanisms—turbulent cavitation in turbomachinery, "rapid phase transition" in spills on hot liquid and solid substrates, contact angle hysteresis, and turbulent free-surfaces in spills on water, with concurrent freezing, condensation, and evaporation phase-change. To assess the ability to simulate such applications, we reviewed lattice Boltzmann methods (LBMs) for stable simulation at high Reynolds numbers including collision operators, boundary conditions, adaptive-mesh refinement, multiphase models, and high-order discretization schemes. As a consequence of these reviewed models having revolved around other fluids than cryogens, the reader will find the scope of this paper to be relatively broad, but our main purpose is to illustrate their capabilities and applicability to cryogenic fluid systems. Conclusively, we showed that there exist few LBM studies that have been dedicated to cryogenic flows, but that the LBM has

25 May 2025 18:08:32

Published under license by AIP Publishing

been extended to simulate many of the phenomena and mechanisms that are found in the physics of cryogenic fluids.

We synthesized the various collision operators that are currently in use, namely single-relaxation and multi-relaxation time (MRT) schemes and entropic stabilizers. The correct implementation of these affects the numerical stability, accuracy, and ability to simulate turbulent flows. Within the last three years significant process was made in formulating MRTs and entropic extensions that can reliably simulate rich turbulent flow fields inspired by many applications. A particular class of LBMs, "simplified and highly stable lattice Boltzmann methods" have proven to significantly reduce memory consumption and enhance computational efficiency and stability. However, these methods should be used with care as they can be diffusive, which may not be appropriate for turbulent flow simulations.

Recent developments in multiphase LBMs have permitted simulating contact angle hysteresis, varying surface chemical potentials—for emulating surface hydrophibicity/philicity—and conjugate heat transfer in fluid–solid couples. We reviewed methods for inferring tunable surface tension, phase transitions, and non-ideal fluid behavior—namely via color-gradient, pseudo-potential, free-energy, and phase-field LBMs. Historically, the LBM has experienced issues with spurious current in interfaces with high curvature, but the aforementioned schemes have all been developed with trivial currents.

Only six studies have employed LBMs specifically for modeling cryogenic fluid systems despite the multiphase-capabilities of the LBM. Available studies have been limited to the color-gradient and pseudo-potential approaches for modeling multiphase flows in cryogenic conditions. The main applications have been fuel-storage for spacecraft, shocks, cavitation, and pool-boiling. With the extreme temperatures in cryogens, we also reviewed models for freezing-phase change relevant to spills on water.

Our primary interest and active area of research is employing our own LBM codes to simulate spill and subsequent pool boiling in various cryogens on both solid and liquid substrates, in order to develop lower-order empirical models for use in larger-scale problems and to provide fundamental insight into the evolution of phase change dynamics in especially the nucleate and transitional regimes.[229,230] Significant challenges exist with developing accurate, deterministic closure models in the hydrodynamic limit and minimizing the inherent computational costs. Especially the baroclinic nature of cryogens has emerged in our previous works.[230] The review provides a roadmap for extending an in-house LBM that has been used for studies on turbulence,[231] porous media flows,[232,233] and microfluidics[234] to allow computationally efficient, large-scale simulations of cryogenic flows.

AUTHORS' CONTRIBUTIONS

K.J.P. conducted the literature survey and composed the manuscript. J.R.B. conceptualized the study and reviewed the manuscript.

ACKNOWLEDGMENTS

We thank our industrial partners Westport Fuel Systems, Fortis BC, BC Ferries, and Port of Vancouver, as well as The Natural Sciences and Engineering Research Council of Canada (NSERC), for funding the research through Collaborative Research Development Grant No. 519885.

DATA AVAILABILITY

Data sharing is not applicable to this article as no new data were created or analyzed in this study.

REFERENCES

[1]N. Rando, "Cryogenics in space," *Observing Photons in Space* (Springer, New York, 2013), pp. 639–655.
[2]Commision of the European Communities, "Green paper: Towards a European strategy for the security of energy supply," Technical Report No. COM (2000) 769 (Brussels, 2000).
[3]M. Momirlan and T. Veziroglu, "Current status of hydrogen energy," Renewable Sustainable Energy Rev. **6**, 141–179 (2002).
[4]R. G. Scurlock, *Stratification, Rollover and Handling of LNG, LPG and Other Cryogenic Liquid Mixtures* (Springer, 2016), p. 250.
[5]American Bureau of Shipping, "LNB Bunkering: Technical and Operational Advisory," Technical Report No. (ABS Houston, Texas, USA, 2014); available at https://ww2.eagle.org/content/dam/eagle/advisories-and-debriefs/ABS_LNG_Bunkering_Advisory.pdf.
[6]M. Shoji, "Studies of boiling chaos: A review," Int. J. Heat Mass Transfer **47**, 1105–1128 (2004).
[7]Y. Utturkar, J. Wu, G. Wang, and W. Shyy, "Recent progress in modeling of cryogenic cavitation for liquid rocket propulsion," Prog. Aerosp. Sci. **41**, 558–608 (2005).
[8]G. H. Yeoh and X. Zhang, "Computational fluid dynamics and population balance modelling of nucleate boiling of cryogenic liquids: Theoretical developments," J. Comput. Multiphase Flows **8**, 178–200 (2016).
[9]P. J. Berenson, "Film-boiling heat transfer from a horizontal surface," J. Heat Transfer **83**, 351–356 (1961).
[10]V. P. Carey, *Liquid-Vapor Phase-Change Phenomena* (CRC Press, 2018).
[11]F. Magaletti, A. Georgoulas, and M. Marengo, "Unraveling low nucleation temperatures in pool boiling through fluctuating hydrodynamics simulations," Int. J. Multiphase Flow **130**, 103356 (2020).
[12]A. Mukherjee and S. G. Kandlikar, "Numerical simulation of growth of a vapor bubble during flow boiling of water in a microchannel," Microfluid. Nanofluid. **1**, 137–145 (2005).
[13]M. Shoji, T. Kohno, J. Negishi, S. Toyoshima, and A. Maeda, "Chaos in boiling on a small-size heater," in Proceedings of the Fourth ASME-JSME Thermal Engineering Joint Conference, Maui (1995), pp. 225–232.
[14]Y. Tatsumi and S. Nishijima, "Effect of helium convection on cryogenic stability of superconducting magnet," IEEE Trans. Appl. Supercond. **13**, 1760–1763 (2003).
[15]N. Schweizer, M. Stelzer, O. Schoele-Schulz, G. Picker, H. Ranebo, J. Dettmann, O. Minster, B. Toth, J. Winter, L. Tadrist, P. Stephan, W. Grassi, P. di Marco, C. Colin, G. Piero Celata, J. Thome, and O. Kabov, "RUBI—a Reference mUltiscale Boiling Investigation for the Fluid Science Laboratory," in *Proceedings of the 38th COSPAR Scientific Assembly*, 15–18 July 2010, Bremen, Germany, p. 18; available at https://ui.adsabs.harvard.edu/abs/2010cosp...38.3565S/abstract
[16]O. Basha, T. Olewski, L. Véchot, M. Castier, and S. Mannan, "Modeling of pool spreading of LNG on land," J. Loss Prev. Process Ind. **30**, 307–314 (2014).
[17]N. Gopalaswami, T. Olewski, L. N. Véchot, and M. S. Mannan, "Small-scale experimental study of vaporization flux of liquid nitrogen released on water," J. Hazard. Mater. **297**, 8–16 (2015).
[18]N. Gopalaswami, L. Véchot, T. Olewski, and M. S. Mannan, "Small-scale experimental study of vaporization flux of liquid nitrogen released on ice," J. Loss Prev. Process Ind. **37**, 124–131 (2015).
[19]J. Schmetz, P. Pili, S. Tjemkes, D. Just, J. Kerkmann, S. Rota, and A. Ratier, "An introduction to Meteosat second generation (MSG)," Bull. Am. Meteorol. Soc. **83**, 992–992 (2002).
[20]H. Chaloupka, M. Hein, G. Müller, and H. Piel, "Research and development of analog HTS microwave components for possible space applications," in ESA/ESTEC Space Applications of High Tc Superconductors (1993), pp. 9–25.
[21]A. Braginski, "Superconducting electronics coming to market," IEEE Trans. Appl. Supercond. **9**, 2825–2836 (1999).

25 May 2025 18:08:32

Published under license by AIP Publishing

[22]L. L. Kohout, "Cryogenic reactant storage for lunar base regenerative fuel cells," in International Conference on Space Power, Cleveland, Ohio, USA (1989).
[23]J. Hardy, Y. Pomeau, and O. de Pazzis, "Time evolution of a two-dimensional classical lattice system," Phys. Rev. Lett. **31**, 276–279 (1973).
[24]C. K. Aidun and J. R. Clausen, "Lattice-Boltzmann method for complex flows," Annu. Rev. Fluid Mech. **42**, 439–472 (2010).
[25]D. Arumuga Perumal and A. K. Dass, "A Review on the development of lattice Boltzmann computation of macro fluid flows and heat transfer," Alexandria Eng. J. **54**, 955–971 (2015).
[26]S. Chen and G. D. Doolen, "Lattice Boltzmann method for fluid flows," Annu. Rev. Fluid Mech. **30**, 329–364 (1998).
[27]Q. Li, K. Luo, Q. Kang, Y. He, Q. Chen, and Q. Liu, "Lattice Boltzmann methods for multiphase flow and phase-change heat transfer," Prog. Energy Combust. Sci. **52**, 62–105 (2016).
[28]C. Cercignani, "Chapter 1: The Boltzmann equation and fluid dynamics," *Handbook of Mathematical Fluid Mechanics*, 1st ed. (North-Holland Press, 2002).
[29]A. R. Harwood, J. O'Connor, J. Sanchez Muñoz, M. C. Santasmasas, and A. J. Revell, "LUMA: A many-core, fluid-structure interaction solver based on the lattice-Boltzmann method," SoftwareX **7**, 88–94 (2018).
[30]J. S. Orr, J. F. Powers, and H. Q. Yang, "Lattice Boltzmann method for spacecraft propellant slosh simulation," in *American Astronautical Society (AAS) Guidance, Navigation, and Control Conference* (National Aeronautics and Space Administration, Breckenridge, CO, USA, 2015).
[31]X. Shan and H. Chen, "Lattice Boltzmann model for simulating flows with multiple phases and components," Phys. Rev. E **47**, 1815–1819 (1993).
[32]Z. Guo and S. Chang, *Lattice Boltzmann Method and Its Applications in Engineering* (World Scientific Publishing Co. Pte. Ltd., Singapore, 2013).
[33]P. L. Bhatnagar, E. P. Gross, and M. Krook, "A model for collision processes in gases. I. Small amplitude processes in charged and neutral one-component systems," Phys. Rev. **94**, 511–525 (1954).
[34]A. Mazloomi, S. S. Chikatamarla, and I. V. Karlin, "Entropic lattice Boltzmann method for multiphase flows: Fluid-solid interfaces," Phys. Rev. E **92**, 023308 (2015).
[35]A. Mazloomi, S. S. Chikatamarla, and I. V. Karlin, "Entropic lattice Boltzmann method for multiphase flows," Phys. Rev. Lett. **114**, 174502 (2015).
[36]G. Pareschi, N. Frapolli, S. S. Chikatamarla, and I. V. Karlin, "Conjugate heat transfer with the entropic lattice Boltzmann method," Phys. Rev. E **94**, 013305 (2016).
[37]I. V. Karlin, A. Ferrante, and H. C. Öttinger, "Perfect entropy functions of the lattice Boltzmann method," Europhys. Lett. **47**, 182–188 (1999).
[38]F. Bösch, S. S. Chikatamarla, and I. V. Karlin, "Entropic multirelaxation lattice Boltzmann models for turbulent flows," Phys. Rev. E **92**, 043309 (2015).
[39]I. V. Karlin, F. Bösch, and S. S. Chikatamarla, "Gibbs' principle for the lattice-kinetic theory of fluid dynamics," Phys. Rev. E **90**, 031302 (2014).
[40]H. E. Morrison and A. Leder, "Sediment transport in turbulent flows with the lattice Boltzmann method," Comput. Fluids **172**, 340–351 (2018).
[41]C. Feuchter, O. Wagner, A. Stief, and T. Beisswenger, "Turbulent flow simulations around a surface-mounted finite cylinder using an entropic multi-relaxation lattice Boltzmann method," Fluid Dyn. Res. **51**, 055509 (2019).
[42]W. Li, Y. Chen, M. Desbrun, C. Zheng, and X. Liu, "Fast and scalable turbulent flow simulation with two-way coupling," ACM Trans. Graph. **39**, 20 (2020).
[43]C. Zhong and A. Komrakova, "Liquid drop breakup in homogeneous isotropic turbulence," Int. J. Numer. Methods Heat Fluid Flow **29**, 2407–2433 (2019).
[44]C.-M. Wu, Y.-S. Zhou, and C.-A. Lin, "Direct numerical simulations of turbulent channel flows with mesh-refinement lattice Boltzmann methods on GPU cluster," Comput. Fluids **210**, 104647 (2020).
[45]L. Xu, F.-B. Tian, J. Young, and J. C. Lai, "A novel geometry-adaptive Cartesian grid based immersed boundary-lattice Boltzmann method for fluid-structure interactions at moderate and high Reynolds numbers," J. Comput. Phys. **375**, 22–56 (2018).
[46]V. Zecevic, M. P. Kirkpatrick, and S. W. Armfield, "Rectangular lattice Boltzmann method using multiple relaxation time collision operator in two and three dimensions," Comput. Fluids **202**, 104492 (2020).
[47]D. D'Humières, "Multiple-relaxation-time lattice Boltzmann models in three dimensions," Philos. Trans. R. Soc. London, Ser. A **360**, 437–451 (2002).
[48]L. A. Hegele, A. Scagliarini, M. Sbragaglia, K. K. Mattila, P. C. Philippi, D. F. Puleri, J. Gounley, and A. Randles, "High-Reynolds-number turbulent cavity flow using the lattice Boltzmann method," Phys. Rev. E **98**, 043302 (2018).
[49]H. Abe, H. Kawamura, and Y. Matsuo, "Direct numerical simulation of a fully developed turbulent channel flow with respect to the Reynolds number dependence," J. Fluids Eng. **123**, 382–393 (2001).
[50]R. D. Moser, J. Kim, and N. N. Mansour, "Direct numerical simulation of turbulent channel flow up to$Re_\tau = 590$," Phys. Fluids **11**, 943–945 (1999).
[51]R. Cornubert, D. D'Humières, and D. Levermore, "A Knudsen layer theory for lattice gases," Physica D **47**, 241–259 (1991).
[52]I. Ginzbourg and P. M. Adler, "Boundary flow condition analysis for the three-dimensional lattice Boltzmann model," J. Phys. II **4**, 191–214 (1994).
[53]D. Kandhai, A. Koponen, A. Hoekstra, M. Kataja, J. Timonen, and P. Sloot, "Implementation aspects of 3D lattice-BGK: Boundaries, accuracy, and a new fast relaxation method," J. Comput. Phys. **150**, 482–501 (1999).
[54]A. J. C. Ladd, "Numerical simulations of particulate suspensions via a discretized Boltzmann equation. Part 1. Theoretical foundation," J. Fluid Mech. **271**, 285–309 (1994).
[55]D. P. Ziegler, "Boundary conditions for lattice Boltzmann simulations," J. Stat. Phys. **71**, 1171–1177 (1993).
[56]C. Peng, O. M. Ayala, and L.-P. Wang, "A comparative study of immersed boundary method and interpolated bounce-back scheme for no-slip boundary treatment in the lattice Boltzmann method: Part I, laminar flows," Comput. Fluids **192**, 104233 (2019).
[57]G.-Q. Chen, X. Huang, A.-M. Zhang, S.-P. Wang, and T. Li, "Three-dimensional simulation of a rising bubble in the presence of spherical obstacles by the immersed boundary lattice Boltzmann method," Phys. Fluids **31**, 097104 (2019).
[58]K. Suzuki, T. Kawasaki, N. Furumachi, Y. Tai, and M. Yoshino, "A thermal immersed boundary-lattice Boltzmann method for moving-boundary flows with Dirichlet and Neumann conditions," Int. J. Heat Mass Transfer **121**, 1099–1117 (2018).
[59]Z. Wang, Y. Wei, and Y. Qian, "A simple direct heating thermal immersed boundary-lattice Boltzmann method for its application in incompressible flow," Comput. Math. Appl. **80**, 1633–1649 (2020).
[60]Z. Guo, B. Shi, and C. Zheng, "A coupled lattice BGK model for the Boussinesq equations," Int. J. Numer. Methods Fluids **39**, 325–342 (2002).
[61]S. Tao, B. Chen, H. Xiao, and S. Huang, "Lattice Boltzmann simulation of thermal flows with complex geometry using a single-node curved boundary condition," Int. J. Therm. Sci. **146**, 106112 (2019).
[62]S. Tao, A. Xu, Q. He, B. Chen, and F. G. Qin, "A curved lattice Boltzmann boundary scheme for thermal convective flows with Neumann boundary condition," Int. J. Heat Mass Transfer **150**, 119345 (2020).
[63]A. Alipour Lalami and A. Hassani Espili, "Two new approaches for applying Neumann boundary condition in thermal lattice Boltzmann method," Comput. Fluids **198**, 104407 (2020).
[64]D. Kenning, "Wall temperature patterns in nucleate boiling," Int. J. Heat Mass Transfer **35**, 73–86 (1992).
[65]S. S. Chikatamarla, S. Ansumali, and I. V. Karlin, "Grad's approximation for missing data in lattice Boltzmann simulations," Europhys. Lett. **74**, 215–221 (2006).
[66]B. Dorschner, S. Chikatamarla, F. Bösch, and I. Karlin, "Grad's approximation for moving and stationary walls in entropic lattice Boltzmann simulations," J. Comput. Phys. **295**, 340–354 (2015).
[67]D. Korba, N. Wang, and L. Li, "Accuracy of interface schemes for conjugate heat and mass transfer in the lattice Boltzmann method," Int. J. Heat Mass Transfer **156**, 119694 (2020).
[68]J. McCullough, C. Leonardi, B. Jones, S. Aminossadati, and J. Williams, "Investigation of local and non-local lattice Boltzmann models for transient heat transfer between non-stationary, disparate media," Comput. Math. Appl. **79**, 174–194 (2020).
[69]Y.-T. Mu, Z.-L. Gu, P. He, and W.-Q. Tao, "Lattice Boltzmann method for conjugated heat and mass transfer with general interfacial conditions," Phys. Rev. E **98**, 043309 (2018).
[70]D. Wang, P. Cheng, and X. Quan, "Photothermal nanobubble nucleation on a plasmonic nanoparticle: A 3D lattice Boltzmann simulation," Int. J. Heat Mass Transfer **140**, 786–797 (2019).

25 May 2025 18:08:32

Published under license by AIP Publishing

[71]J. W. Cahn, "Critical point wetting," J. Chem. Phys. **66**, 3667–3672 (1977).
[72]E. Cheng, G. Mistura, H. C. Lee, M. H. W. Chan, M. W. Cole, C. Carraro, W. F. Saam, and F. Toigo, "Wetting transitions of liquid hydrogen films," Phys. Rev. Lett. **70**, 1854–1857 (1993).
[73]G. B. Hess, M. J. Sabatini, and M. H. W. Chan, "Nonwetting of cesium by neon near its critical point," Phys. Rev. Lett. **78**, 1739–1742 (1997).
[74]J. Klier, P. Stefanyi, and A. F. G. Wyatt, "Contact angle of liquid He-4 on a Cs surface," Phys. Rev. Lett. **75**, 3709–3712 (1995).
[75]D. Ross, J. E. Rutledge, and P. Taborek, "Triple point dewetting transitions of helium mixtures on cesium," Phys. Rev. Lett. **76**, 2350–2353 (1996).
[76]D. Ross, P. Taborek, and J. E. Rutledge, "Wetting behavior of He-2 on cesium," Phys. Rev. B **58**, R4274–R4276 (1998).
[77]J. E. Rutledge and P. Taborek, "Prewetting phase diagram of He-4 on cesium," Phys. Rev. Lett. **69**, 937–940 (1992).
[78]R. Bausch, R. Blossey, and M. A. Burschka, "Critical nuclei for wetting and dewetting," J. Phys. A **27**, 1405–1406 (1994).
[79]D. Bonn, H. Kellay, and J. Meunier, "Metastable states and nucleation near first-order wetting transitions," Phys. Rev. Lett. **73**, 3560–3563 (1994).
[80]D. Bonn, E. Bertrand, J. Meunier, and R. Blossey, "Dynamics of wetting layer formation," Phys. Rev. Lett. **84**, 4661–4664 (2000).
[81]M. Schick and P. Taborek, "Anomalous nucleation at first-order wetting transitions," Phys. Rev. B **46**, 7312–7314 (1992).
[82]I. Pioro, W. Rohsenow, and S. Doerffer, "Nucleate pool-boiling heat transfer. I: Review of parametric effects of boiling surface," Int. J. Heat Mass Transfer **47**, 5033–5044 (2004).
[83]B. Wen, X. Zhou, B. He, C. Zhang, and H. Fang, "Chemical-potential-based lattice Boltzmann method for nonideal fluids," Phys. Rev. E **95**, 1–7 (2017).
[84]R. Benzi, L. Biferale, M. Sbragaglia, S. Succi, and F. Toschi, "Mesoscopic modeling of a two-phase flow in the presence of boundaries: The contact angle," Phys. Rev. E **74**, 021509 (2006).
[85]Q. Li, K. H. Luo, Q. J. Kang, and Q. Chen, "Contact angles in the pseudopotential lattice Boltzmann modeling of wetting," Phys. Rev. E **90**, 053301 (2014).
[86]N. S. Martys and H. Chen, "Simulation of multicomponent fluids in complex three-dimensional geometries by the lattice Boltzmann method," Phys. Rev. E **53**, 743–750 (1996).
[87]Q. Kang, D. Zhang, and S. Chen, "Displacement of a two-dimensional immiscible droplet in a channel," Phys. Fluids **14**, 3203–3214 (2002).
[88]P. Raiskinmaki, A. Koponen, J. Merikoski, and J. Timonen, "Spreading dynamics of three-dimensional droplets by the lattice-Boltzmann method," Comput. Mater. Sci. **18**, 7–12 (2000).
[89]J. Yang, X. Ma, L. Fei, X. Zhang, K. H. Luo, and S. Shuai, "Effects of hysteresis window on contact angle hysteresis behaviour at large bond number," J. Colloid Interface Sci. **566**, 327–337 (2020).
[90]A. Urbano, S. Tanguy, G. Huber, and C. Colin, "Direct numerical simulation of nucleate boiling in micro-layer regime," Int. J. Heat Mass Transfer **123**, 1128–1137 (2018).
[91]M. Watari and M. Tsutahara, "Two-dimensional thermal model of the finite-difference lattice Boltzmann method with high spatial isotropy," Phys. Rev. E **67**, 036306 (2003).
[92]G. Gonnella, A. Lamura, and V. Sofonea, "Lattice Boltzmann simulation of thermal nonideal fluids," Phys. Rev. E **76**, 036703 (2007).
[93]V. Sofonea, "Implementation of diffuse reflection boundary conditions in a thermal lattice Boltzmann model with flux limiters," J. Comput. Phys. **228**, 6107–6118 (2009).
[94]T. Traudt and S. Schlechtriem, "Validation of a lattice Boltzmann model for transient cryogenic two-phase flow," Trans. Jpn. Soc. Aeronaut. Space Sci., Aerosp. Technol. Jpn. **17**, 321–326 (2019).
[95]J. C. Maxwell, "VII. On stresses in rarified gases arising from inequalities of temperature," Philos. Trans. R. Soc. London **170**, 231–256 (1879).
[96]O. Filippova and D. Hanel, "Grid refinement for lattice-BGK models," J. Comput. Phys. **147**, 219–228 (1998).
[97]D. Lagrava, O. Malaspinas, J. Latt, and B. Chopard, "Advances in multi-domain lattice Boltzmann grid refinement," J. Comput. Phys. **231**, 4808–4822 (2012).
[98]T.-M. Liou and C.-S. Wang, "Three-dimensional multidomain lattice Boltzmann grid refinement for passive scalar transport," Phys. Rev. E **98**, 013306 (2018).
[99]D. Yu, R. Mei, and W. Shyy, "A multi-block lattice Boltzmann method for viscous fluid flows," Int. J. Numer. Methods Fluids **39**, 99–120 (2002).
[100]R. S. Baker, "A block adaptive mesh refinement algorithm for the neutral particle transport equation," Nucl. Sci. Eng. **141**, 1–12 (2002).
[101]S. M. Guzik, T. H. Weisgraber, P. Colella, and B. J. Alder, "Interpolation methods and the accuracy of lattice-Boltzmann mesh refinement," J. Comput. Phys. **259**, 461–487 (2014).
[102]R. L. Tellier, D. Fournier, and C. Suteau, "Reactivity perturbation formulation for a discontinuous Galerkin-based transport solver and its use with adaptive mesh refinement," Nucl. Sci. Eng. **167**, 209–220 (2011).
[103]Y. Ma, Y. Wang, and M. Xie, "Multiblock adaptive mesh refinement for the SN transport equation based on lattice Boltzmann method," Nucl. Sci. Eng. **193**, 1219–1237 (2019).
[104]Y. Wang, M. Xie, and Y. Ma, "Neutron transport solution of lattice Boltzmann method and streaming-based block-structured adaptive mesh refinement," Ann. Nucl. Energy **118**, 249–259 (2018).
[105]Y. Wang, X. Peng, M. Xie, and Y. Ma, "High-order lattice Boltzmann framework and its adaptive mesh refinement in the neutron transport SP3 solutions," Prog. Nucl. Energy **128**, 103449 (2020).
[106]F. Schornbaum and U. Rüde, "Extreme-scale block-structured adaptive mesh refinement," SIAM J. Sci. Comput. **40**, C358–C387 (2018).
[107]M. Bauer, S. Eibl, C. Godenschwager, N. Kohl, M. Kuron, C. Rettinger, F. Schornbaum, C. Schwarzmeier, D. Thönnes, H. Köstler, and U. Rüde, "waLBerla: A block-structured high-performance framework for multiphysics simulations," Comput. Math. Appl. **81**, 478–501 (2021).
[108]L. Li, C. Xu, C. Shi, X. Han, and W. Shen, "Investigation of wake characteristics of the MEXICO wind turbine using lattice Boltzmann method," Wind Energy **24**, 116–132 (2021).
[109]C. Zhang, A. Fakhari, J. Li, L.-S. Luo, and T. Qian, "A comparative study of interface-conforming ALE-FE scheme and diffuse interface AMR-LB scheme for interfacial dynamics," J. Comput. Phys. **395**, 602–619 (2019).
[110]A. Zhang, J. Du, Z. Guo, Q. Wang, and S. Xiong, "Conservative phase-field method with a parallel and adaptive-mesh-refinement technique for interface tracking," Phys. Rev. E **100**, 023305 (2019).
[111]F.-S. Hsu, K.-C. Chang, and M. Smith, "Multi-block adaptive mesh refinement (AMR) for a lattice Boltzmann solver using GPUs," Comput. Fluids **175**, 48–52 (2018).
[112]N. Onodera, Y. Idomura, Y. Ali, and, and T. Shimokawabe, "Communication reduced multi-time-step algorithm for real-time wind simulation on GPU-based supercomputers," in *2018 IEEE/ACM 9th Workshop on Latest Advances in Scalable Algorithms for Large-Scale Systems (scalA)* (IEEE, 2018), pp. 9–16.
[113]X. Zhang, J. Kang, Z. Guo, and Q. Han, "Effect of the forced flow on the permeability of dendritic networks: A study using phase-field-lattice Boltzmann method," Int. J. Heat Mass Transfer **131**, 196–205 (2019).
[114]A. K. Gunstensen, D. H. Rothman, S. Zaleski, and G. Zanetti, "Lattice Boltzmann model of immiscible fluids," Phys. Rev. A **43**, 4320–4327 (1991).
[115]D. H. Rothman and J. M. Keller, "Immiscible cellular-automaton fluids," J. Stat. Phys. **52**, 1119–1127 (1988).
[116]S. V. Lishchuk, C. M. Care, and I. Halliday, "Lattice Boltzmann algorithm for surface tension with greatly reduced microcurrents," Phys. Rev. E **67**, 036701 (2003).
[117]M. Latva-Kokko and D. H. Rothman, "Diffusion properties of gradient-based lattice Boltzmann models of immiscible fluids," Phys. Rev. E **71**, 056702 (2005).
[118]Y. Ba, H. Liu, Q. Li, Q. Kang, and J. Sun, "Multiple-relaxation-time color-gradient lattice Boltzmann model for simulating two-phase flows with high density ratio," Phys. Rev. E **94**, 023310 (2016).
[119]Z. Guo, C. Zheng, and B. Shi, "Discrete lattice effects on the forcing term in the lattice Boltzmann method," Phys. Rev. E **65**, 046308 (2002).
[120]I. Halliday, A. P. Hollis, and C. M. Care, "Lattice Boltzmann algorithm for continuum multicomponent flow," Phys. Rev. E **76**, 026708 (2007).
[121]T. Reis and T. N. Phillips, "Lattice Boltzmann model for simulating immiscible two-phase flows," J. Phys. A **40**, 4033–4053 (2007).
[122]S. Leclaire, M. Reggio, and J.-Y. Trépanier, "Numerical evaluation of two recoloring operators for an immiscible two-phase flow lattice Boltzmann model," Appl. Math. Modell. **36**, 2237–2252 (2012).

25 May 2025 18:08:32

Published under license by AIP Publishing

[123]A. Gupta and R. Kumar, "Effect of geometry on droplet formation in the squeezing regime in a microfluidic T-junction," Microfluid. Nanofluid. **8**, 799–812 (2010).
[124]H. Liu, A. J. Valocchi, and Q. Kang, "Three-dimensional lattice Boltzmann model for immiscible two-phase flow simulations," Phys. Rev. E **85**, 046309 (2012).
[125]Z. X. Wen, Q. Li, Y. Yu, and K. H. Luo, "Improved three-dimensional color-gradient lattice Boltzmann model for immiscible two-phase flows," Phys. Rev. E **100**, 023301 (2019).
[126]J. Tölke, "Lattice Boltzmann simulations of binary fluid flow through porous media," Philos. Trans. R. Soc. London, Ser. A **360**, 535–545 (2002).
[127]H. Huang, J. J. Huang, X. Y. Lu, and M. C. Sukop, "On simulations of high-density ratio flows using color-gradient multiphase lattice Boltzmann models," Int. J. Mod. Phys. C **24**, 1350021–1350019 (2013).
[128]T. Inamuro, N. Konishi, and F. Ogino, "Galilean invariant model of the lattice Boltzmann method for multiphase fluid flows using free-energy approach," Comput. Phys. Commun. **129**, 32–45 (2000).
[129]A. N. Kalarakis, V. N. Burganos, and A. C. Payatakes, "Galilean-invariant lattice-Boltzmann simulation of liquid-vapor interface dynamics," Phys. Rev. E **65**, 056702 (2002).
[130]Y. K. Lee and K. H. Ahn, "Particle dynamics at fluid interfaces studied by the color gradient lattice Boltzmann method coupled with the smoothed profile method," Phys. Rev. E **101**, 053302 (2020).
[131]X. Shan and H. Chen, "Simulation of nonideal gases and liquid-gas phase transitions by the lattice Boltzmann equation," Phys. Rev. E **49**, 2941–2948 (1994).
[132]J. Chin, "Lattice Boltzmann simulation of the flow of binary immiscible fluids with different viscosities using the Shan-Chen microscopic interaction model," Philos. Trans. R. Soc. London, Ser. A **360**, 547–558 (2002).
[133]Q. Kang, D. Zhang, and S. Chen, "Immiscible displacement in a channel: Simulations of fingering in two dimensions," Adv. Water Resour. **27**, 13–22 (2004).
[134]R. Zhang, X. He, G. Doolen, and S. Chen, "Surface tension effects on two-dimensional two-phase Kelvin-Helmholtz instabilities," Adv. Water Resour. **24**, 461–478 (2001).
[135]P. Yuan and L. Schaefer, "Equations of state in a lattice Boltzmann model," Phys. Fluids **18**, 042101 (2006).
[136]P. C. Kwok, "Green's function method in lattice dynamics," Solid-State Phys. **20**, 213–303 (1968).
[137]J. Sun, J. Gong, and G. Li, "A lattice Boltzmann model for solidification of water droplet on cold flat plate," Int. J. Refrig. **59**, 53–64 (2015).
[138]E. Reyhanian, B. Dorschner, and I. Karlin, "Thermokinetic model of compressible multiphase flows," arXiv:2002.09217 (2020).
[139]G. Zhao-Li, Z. Chu-Guang, and S. Bao-Chang, "Non-equilibrium extrapolation method for velocity and pressure boundary conditions in the lattice Boltzmann method," Chin. Phys. **11**, 366–374 (2002).
[140]Q. Li and K. H. Luo, "Achieving tunable surface tension in the pseudopotential lattice Boltzmann modeling of multiphase flows," Phys. Rev. E **88**, 053307 (2013).
[141]P. Zhou, W. Liu, and Z. Liu, "Lattice Boltzmann simulation of nucleate boiling in micro-pillar structured surface," Int. J. Heat Mass Transfer **131**, 1–10 (2019).
[142]P. Zhou, Z. Liu, W. Liu, and X. Duan, "LBM simulates the effect of sole nucleate site geometry on pool boiling," Appl. Therm. Eng. **160**, 114027 (2019).
[143]W. Z. Fang, L. Chen, Q. J. Kang, and W. Q. Tao, "Lattice Boltzmann modeling of pool boiling with large liquid-gas density ratio," Int. J. Therm. Sci. **114**, 172–183 (2017).
[144]S. Gong and P. Cheng, "Direct numerical simulations of pool boiling curves including heater's thermal responses and the effect of vapor phase's thermal conductivity," Int. Commun. Heat Mass Transfer **87**, 61–71 (2017).
[145]X. Ma, P. Cheng, and X. Quan, "Simulations of saturated boiling heat transfer on bio-inspired two-phase heat sinks by a phase-change lattice Boltzmann method," Int. J. Heat Mass Transfer **127**, 1013–1024 (2018).
[146]P. Berghout and H. E. Van den Akker, "Simulating drop formation at an aperture by means of a multi-component pseudo-potential lattice Boltzmann model," Int. J. Heat Fluid Flow **75**, 153–164 (2019).
[147]E. Ezzatneshan and H. Vaseghnia, "Simulation of collapsing cavitation bubbles in various liquids by lattice Boltzmann model coupled with the Redlich-Kwong-Soave equation of state," Phys. Rev. E **102**, 053309 (2020).
[148]G. Falcucci, E. Jannelli, S. Ubertini, and S. Succi, "Direct numerical evidence of stress-induced cavitation," J. Fluid Mech. **728**, 362–375 (2013).
[149]Y. Liu and Y. Peng, "Study on the collapse process of cavitation bubbles near the concave wall by lattice Boltzmann method pseudo-potential model," Energies **13**, 4398 (2020).
[150]H. Peng, J. Zhang, X. He, and Y. Wang, "Thermal pseudo-potential lattice Boltzmann method for simulating cavitation bubbles collapse near a rigid boundary," Comput. Fluids **217**, 104817 (2021).
[151]A. Hu, R. Uddin, and D. Liu, "Discrete methods of the energy equations in the pseudo-potential lattice Boltzmann model based simulations," Comput. Fluids **179**, 645–654 (2019).
[152]G. Barakos, E. Mitsoulis, and D. Assimacopoulos, "Natural convection flow in a square cavity revisited: Laminar and turbulent models with wall functions," Int. J. Numer. Methods Fluids **18**, 695–719 (1994).
[153]E. Reyhanian, B. Dorschner, and I. Karlin, "Kinetic simulations of compressible non-ideal fluids: From supercritical to phase-change and exotic behavior," arXiv:2012.01313 (2020).
[154]J. W. Grove, "Some comments on thermodynamic consistency for equilibrium mixture equations of state," Comput. Math. Appl. **78**, 582–597 (2019).
[155]R. Menikoff and B. J. Plohr, "The Riemann problem for fluid flow of real materials," Rev. Mod. Phys. **61**, 75–130 (1989).
[156]E. Orlandini, M. R. Swift, and J. M. Yeomans, "A lattice Boltzmann model of binary-fluid mixtures," Europhys. Lett. **32**, 463–468 (1995).
[157]M. R. Swift, W. R. Osborn, and J. M. Yeomans, "Lattice Boltzmann simulation of nonideal fluids," Phys. Rev. Lett. **75**, 830–833 (1995).
[158]M. R. Swift, E. Orlandini, W. R. Osborn, and J. M. Yeomans, "Lattice Boltzmann simulations of liquid-gas and binary fluid systems," Phys. Rev. E **54**, 5041–5052 (1996).
[159]B. Rowlinson and J. S. Widom, *Molecular Theory of Capillarity* (Courier Corporation, 1983).
[160]H. W. Zheng, C. Shu, and Y. T. Chew, "Lattice Boltzmann interface capturing method for incompressible flows," Phys. Rev. E **72**, 056705 (2005).
[161]H. Zheng, C. Shu, and Y. Chew, "A lattice Boltzmann model for multiphase flows with large density ratio," J. Comput. Phys. **218**, 353–371 (2006).
[162]U. Frisch, B. Hasslacher, and Y. Pomeau, "Lattice-gas automata for the Navier-Stokes equation," Phys. Rev. Lett. **56**, 1505–1508 (1986).
[163]B. Wen, Z. Qin, C. Zhang, and H. Fang, "Thermodynamic-consistent lattice Boltzmann model for nonideal fluids," Europhys. Lett. **112**, 44002 (2015).
[164]T. Inamuro, T. Ogata, S. Tajima, and N. Konishi, "A lattice Boltzmann method for incompressible two-phase flows with large density differences," J. Comput. Phys. **198**, 628–644 (2004).
[165]M. Wöhrwag, C. Semprebon, A. Mazloomi Moqaddam, I. Karlin, and H. Kusumaatmaja, "Ternary free-energy entropic lattice Boltzmann model with a high density ratio," Phys. Rev. Lett. **120**, 234501 (2018).
[166]N. Bala, M. Pepona, I. Karlin, H. Kusumaatmaja, and C. Semprebon, "Wetting boundaries for a ternary high-density-ratio lattice Boltzmann method," Phys. Rev. E **100**, 013308 (2019).
[167]J. Bao and L. Schaefer, "Lattice Boltzmann equation model for multi-component multi-phase flow with high density ratios," Appl. Math. Modell. **37**, 1860–1871 (2013).
[168]H. Liang, B. C. Shi, and Z. H. Chai, "Lattice Boltzmann modeling of three-phase incompressible flows," Phys. Rev. E **93**, 013308 (2016).
[169]C. Semprebon, T. Krüger, and H. Kusumaatmaja, "Ternary free-energy lattice Boltzmann model with tunable surface tensions and contact angles," Phys. Rev. E **93**, 033305 (2016).
[170]F. Boyer and C. Lapuerta, "Study of a three component Cahn-Hilliard flow model," ESAIM **40**, 653–687 (2006).
[171]R. H. H. Abadi, M. H. Rahimian, and A. Fakhari, "Conservative phase-field lattice-Boltzmann model for ternary fluids," J. Comput. Phys. **374**, 668–691 (2018).
[172]S. M. Allen and J. W. Cahn, "Mechanisms of phase transformations within the miscibility gap of Fe-rich Fe-Al alloys," Acta Metall. **24**, 425–437 (1976).
[173]J. W. Cahn and J. E. Hilliard, "Free energy of a nonuniform system. I. Interfacial free energy," J. Chem. Phys. **28**, 258–267 (1958).
[174]F. Bornemann, "Accuracy and stability of computing high-order derivatives of analytic functions by Cauchy integrals," Found. Comput. Math. **11**, 1–63 (2011).

25 May 2025 18:08:32

Published under license by AIP Publishing

[175]G. Miel and R. Mooney, "On the condition number of Lagrangian numerical differentiation," Appl. Math. Comput. **16**, 241–252 (1985).
[176]P.-H. Chiu and Y.-T. Lin, "A conservative phase field method for solving incompressible two-phase flows," J. Comput. Phys. **230**, 185–204 (2011).
[177]M. Geier, A. Fakhari, and T. Lee, "Conservative phase-field lattice Boltzmann model for interface tracking equation," Phys. Rev. E **91**, 063309 (2015).
[178]S. Dai and Q. Du, "Computational studies of coarsening rates for the Cahn-Hilliard equation with phase-dependent diffusion mobility," J. Comput. Phys. **310**, 85–108 (2016).
[179]P. M. Dupuy, M. Fernandino, H. A. Jakobsen, and H. F. Svendsen, "Using Cahn-Hilliard mobility to simulate coalescence dynamics," Comput. Math. Appl. **59**, 2246–2259 (2010).
[180]D. Jacqmin, "Calculation of two-phase Navier-Stokes flows using phase-field modeling," J. Comput. Phys. **155**, 96–127 (1999).
[181]J. Zhu, L.-Q. Chen, J. Shen, and V. Tikare, "Coarsening kinetics from a variable-mobility Cahn-Hilliard equation: Application of a semi-implicit Fourier spectral method," Phys. Rev. E **60**, 3564–3572 (1999).
[182]A. Fakhari, T. Mitchell, C. Leonardi, and D. Bolster, "Improved locality of the phase-field lattice-Boltzmann model for immiscible fluids at high density ratios," Phys. Rev. E **96**, 053301 (2017).
[183]R. Sadeghi and M. S. Shadloo, "Three-dimensional numerical investigation of film boiling by the lattice Boltzmann method," Numer. Heat Transfer, Part A **71**, 560–574 (2017).
[184]V. V. Klimenko, "Film boiling on a horizontal plate—new correlation," Int. J. Heat Mass Transfer **24**, 69–79 (1981).
[185]C. Ma, J. Wu, and T. Zhang, "A high order spectral difference-based phase field lattice Boltzmann method for incompressible two-phase flows," Phys. Fluids **32**, 122113 (2020).
[186]R. Kalantarpour, A. Ebadi, S. M. Hosseinalipour, and H. Liang, "Three-component phase-field lattice Boltzmann method with high density ratio and ability to simulate total spreading states," Comput. Fluids **204**, 104480 (2020).
[187]Y. P. Sitompul, T. Aoki, and T. Takaki, "Simulation of turbulent bubbly pipe flow with high density ratio and high Reynolds number by using the lattice Boltzmann method and a multi-phase field model," Int. J. Multiphase Flow **134**, 103505 (2021).
[188]F. O. Alpak, I. Zacharoudiou, S. Berg, J. Dietderich, and N. Saxena, "Direct simulation of pore-scale two-phase visco-capillary flow on large digital rock images using a phase-field lattice Boltzmann method on general-purpose graphics processing units," Comput. Geosci. **23**, 849–880 (2019).
[189]S. Sakane and T. Takaki, "Phase-field lattice Boltzmann method with two-relaxation-time model for dendrite growth of a binary alloy with melt convection," Comput. Mater. Sci. **186**, 110070 (2021).
[190]S. Meng, A. Zhang, Z. Guo, and Q. Wang, "Phase-field-lattice Boltzmann simulation of dendrite motion using an immersed boundary method," Comput. Mater. Sci. **184**, 109784 (2020).
[191]S. Ansumali and I. V. Karlin, "Kinetic boundary conditions in the lattice Boltzmann method," Phys. Rev. E **66**, 026311 (2002).
[192]F. J. Higuera and J. Jimenez, "Boltzmann approach to lattice gas simulations," Europhys. Lett. **9**, 663–668 (1989).
[193]H. Yoshida and M. Nagaoka, "Multiple-relaxation-time lattice Boltzmann model for the convection and anisotropic diffusion equation," J. Comput. Phys. **229**, 7774–7795 (2010).
[194]Z. Chen, C. Shu, and D. Tan, "Highly accurate simplified lattice Boltzmann method," Phys. Fluids **30**, 103605 (2018).
[195]Z. Chen, C. Shu, and D. Tan, "Three-dimensional simplified and unconditionally stable lattice Boltzmann method for incompressible isothermal and thermal flows," Phys. Fluids **29**, 053601 (2017).
[196]Z. Chen, C. Shu, and D. Tan, "A truly second-order and unconditionally stable thermal lattice Boltzmann method," Appl. Sci. **7**, 277 (2017).
[197]Z. Chen, C. Shu, and D. Tan, "Immersed boundary-simplified lattice Boltzmann method for incompressible viscous flows," Phys. Fluids **30**, 053601 (2018).
[198]Z. Chen, C. Shu, D. Tan, and C. Wu, "On improvements of simplified and highly stable lattice Boltzmann method: Formulations, boundary treatment, and stability analysis," Int. J. Numer. Methods Fluids **87**, 161–179 (2018).
[199]Z. Chen and C. Shu, "On numerical diffusion of simplified lattice Boltzmann method," Int. J. Numer. Methods Fluids **92**, 1198–1211 (2020).
[200]Z. Chen and C. Shu, "Simplified lattice Boltzmann method for non-Newtonian power-law fluid flows," Int. J. Numer. Methods Fluids **92**, 38–54 (2020).
[201]Z. Chen, C. Shu, L. M. Yang, X. Zhao, and N. Y. Liu, "Immersed boundary-simplified thermal lattice Boltzmann method for incompressible thermal flows," Phys. Fluids **32**, 013605 (2020).
[202]Y. Ma and Z. Yang, "Simplified and highly stable thermal Lattice Boltzmann method simulation of hybrid nanofluid thermal convection at high Rayleigh numbers," Phys. Fluids **32**, 012009 (2020).
[203]Q.-Z. Li, Z.-L. Lu, D. Zhou, X.-D. Niu, T.-Q. Guo, and B.-C. Du, "Unified simplified multiphase lattice Boltzmann method for ferrofluid flows and its application," Phys. Fluids **32**, 093302 (2020).
[204]X. Li, Z.-Q. Dong, P. Yu, X.-D. Niu, L.-P. Wang, D.-C. Li, and H. Yamaguchi, "Numerical investigation of magnetic multiphase flows by the fractional-step-based multiphase lattice Boltzmann method," Phys. Fluids **32**, 083309 (2020).
[205]A. Khan, X.-D. Niu, Q.-Z. Li, Y. Li, D. Li, and H. Yamaguchi, "Dynamic study of ferrodroplet and bubbles merging in ferrofluid by a simplified multiphase lattice Boltzmann method," J. Magn. Magn. Mater. **495**, 165869 (2020).
[206]Y. Wang, C. Zhong, J. Cao, C. Zhuo, and S. Liu, "A simplified finite volume lattice Boltzmann method for simulations of fluid flows from laminar to turbulent regime, part II: Extension towards turbulent flow simulation," Comput. Math. Appl. **79**, 2133–2152 (2020).
[207]Y. Wang, C. Zhong, J. Cao, C. Zhuo, and S. Liu, "A simplified finite volume lattice Boltzmann method for simulations of fluid flows from laminar to turbulent regime, part I: Numerical framework and its application to laminar flow simulation," Comput. Math. Appl. **79**, 1590–1618 (2020).
[208]Y. Izumi, A. Iwamoto, Y. Tatsumi, S. Takeda, and S. Nishijima, "Lattice Boltzmann method analyzing helium bubbles motion in liquid helium," IEEE Trans. Appl. Supercond. **14**, 1326–1329 (2004).
[209]A. R. Imre, G. Mayer, G. Házi, R. Rozas, and T. Kraska, "Estimation of the liquid-vapor spinodal from interfacial properties obtained from molecular dynamics and lattice Boltzmann simulations," J. Chem. Phys. **128**, 114708 (2008).
[210]NIST, *NIST Chemistry WebBook* (NIST, 2018).
[211]D. Or and M. Tuller, "Cavitation during desaturation of porous media under tension," Water Resour. Res. **38**, 19-1–19-14, https://doi.org/10.1029/2001WR000282 (2002).
[212]M. S. Plesset and A. Prosperetti, "Bubble dynamics and cavitation," Annu. Rev. Fluid Mech. **9**, 145–185 (1977).
[213]A. Kupershtokh, "New method of incorporating a body force term into the lattice Boltzmann equation," in 5th International EHD Workshop, Poitiers, France (2004).
[214]M. Watari and M. Tsutahara, "Supersonic flow simulations by a three-dimensional multispeed thermal model of the finite difference lattice Boltzmann method," Physica A **364**, 129–144 (2006).
[215]S. Wagner, "Vorlesung Strömungslehre," Ph.D. thesis (Universität Stuttgart, 2005).
[216]Y. Peng, B. Wang, and Y. Mao, "Study on force schemes in pseudopotential lattice Boltzmann model for two-phase flows," Math. Probl. Eng. **2018**, 6496379.
[217]M. Dular and M. Petkovšek, "Cavitation erosion in liquid nitrogen," Wear **400-401**, 111–118 (2018).
[218]B. E. Poiling, J. M. Prausnitz, and J. P. O'Connell, *The Properties of Gases and Liquids*, 5th ed. (McGraw-Hill, New York, 2001).
[219]D. H. Travena, *Cavitation and Tension in Liquids* (Hilger, Bristol, Philadelphia, 1987).
[220]X. Li, J. Zhao, and P. Cheng, "A lattice Boltzmann model for condensation and freezing of dry saturated vapor about a cryogenic spot on an inclined hydrophobic surface," Int. J. Heat Mass Transfer **114**, 628–639 (2017).
[221]J. Zhao, X. Li, and P. Cheng, "Lattice Boltzmann simulation of a droplet impact and freezing on cold surfaces," Int. Commun. Heat Mass Transfer **87**, 175–182 (2017).
[222]S. R. Friedman, M. Khalil, and P. Taborek, "Wetting transition in water," Phys. Rev. Lett. **111**, 226101 (2013).
[223]E. Cheng, M. W. Cole, W. F. Saam, and J. Treiner, "Helium prewetting and nonwetting on weak-binding substrates," Phys. Rev. Lett. **67**, 1007–1010 (1991).

25 May 2025 18:08:32

Published under license by AIP Publishing

[224]M. Frank, M. Papanikolaou, D. Drikakis, and K. Salonitis, "Heat transfer across a fractal surface," J. Chem. Phys. **151**, 134705 (2019).
[225]Q. He, Y. Li, W. Huang, Y. Hu, D. Li, and Y. Wang, "A unified lattice Boltzmann model for immiscible and miscible ternary fluids," Comput. Math. Appl. **80**, 2830–2859 (2020).
[226]L. Vienne, S. Marie, and F. Grasso, "Lattice Boltzmann method for miscible gases: A forcing-term approach," Phys. Rev. E **100**, 023309 (2019).
[227]I. Kostin, M. Marion, R. Texier-Picard, and V. A. Volpert, "Modelling of miscible liquids with the Korteweg stress," ESAIM **37**, 741–753 (2003).
[228]Y. Sugii, K. Okamoto, A. Hibara, M. Tokeshi, and T. Kitamori, "Effect of Korteweg stress in miscible liquid two-layer flow in a microfluidic device," J. Visualization **8**, 117–124 (2005).
[229]S. Rahbarimanesh, J. Brinkerhoff, and J. Huang, "Development and validation of a homogeneous flow model for simulating cavitation in cryogenic fluids," Appl. Math. Modell. **56**, 584–611 (2018).
[230]S. Rahbarimanesh and J. Brinkerhoff, "A numerical study on the effects of cavitation number on cavitating mixing layer of liquefied natural gas (LNG) behind a flat plate splitter," in 10th International Symposium on Cavitation (2018).
[231]C.-S. Wang and T.-M. Liou, "Lattice Boltzmann simulation of turbulent flow in rotating rectangular ducts with various aspect ratios," Phys. Rev. Fluids **5**, 124608 (2020).
[232]C.-S. Wang and J. Brinkerhoff, "Advances in mathematical modeling of hydrogen adsorption and desorption in metal hydride beds with lattice Boltzmann method," Int. J. Hydrogen Energy **45**, 32179–32195 (2020).
[233]C.-S. Wang, P.-Y. Shen, and T.-M. Liou, "A consistent thermal lattice Boltzmann method for heat transfer in arbitrary combinations of solid, fluid, and porous media," Comput. Methods Appl. Mech. Eng. **368**, 113200 (2020).
[234]T.-M. Liou, T.-C. Wei, and C.-S. Wang, "Investigation of nanofluids on heat transfer enhancement in a louvered microchannel with lattice Boltzmann method," J. Therm. Anal. Calorim. **135**, 751–762 (2019).

25 May 2025 18:08:32

Published under license by AIP Publishing